*VOR (version of record)

[redacted]

A portable six-wheeled mobile robot with reconfigurable body and self-adaptable obstacle-climbing mechanisms

Zhen Song [1], Zirong Luo [1], Guowu Wei [2], Jianzhong Shang[1]

[1] College of Mechatronic Engineering and Automation, National University of Defense Technology, Changsha 410073, PR China

[2] School of Science, Engineering and Environment, University of Salford, Salford M5 4WT, United Kingdom

Correspondence to: Zirong Luo (luozirong@nudt.edu.cn), Guowu Wei (g.wei@salford.ac.uk)

Abstract: Mobile robots can replace rescuers in rescue and detection missions in complex and unstructured environments and draw the interest of many researchers. This paper presents a novel six-wheeled mobile robot with a reconfigurable body and self-adaptable obstacle-climbing mechanisms, which can reconfigure itself to three locomotion states to realize the advantages of terrain adaptability, obstacle crossing ability and portability. Design criteria and mechanical design of the proposed mobile robot are firstly presented, based on which the geometry of the robot is modelled and the geometric constraint, static conditions and motion stability condition for obstacle crossing of the robot are derived and formulated. Numerical simulations are then conducted to verify the geometric passing capability, static passing capability and motion stability and find feasible structure parameters of the robot in obstacle crossing. Further, a physical prototype of the proposed mobile robot is developed and integrated with mechatronic systems and remote control. Using the prototype, field experiments are carried out to verify the feasibility of the proposed design and theoretical derivations. The results show that the proposed mobile robot satisfies all the criteria set and is feasible for applications in disastrous rescuing scenarios.

Keywords: Reconfigurable robot; six-wheeled mobile robot; self-adaptive climbing mechanism; obstacle crossing

1. Introduction

Frequent natural and man-caused disasters, such as earthquake, radiation and explosion, seriously threaten the security and lives of human society [1, 2]. The situation in disastrous scenarios is always complex and changeable, which is easy to cause secondary injury to rescuers and trapped people. To reduce the potential risk, mobile robots have been regarded as an effective method in such cases to replace rescuers for life detection in unstructured and rugged environments.

However, at present, the application of mobile robots in disaster rescue is not mature enough, and there are still some technical problems that have not been solved, such as low working and energy efficiency, low mobility in harsh environments, large volume, large quality, and inconvenience for transportation. The rugged and complex terrain environment in disastrous scenarios also requires the

robots to have excellent terrain adaptability and obstacle-crossing ability [3, 4]. Therefore, it is of great value and significance to develop a ground mobile robot with simple structure, low energy consumption, and outstanding obstacle-crossing ability and terrain adaptability [5, 6]. The purpose of this paper is to design a portable robot with simple structure and control for natural disaster rescue.

The potential solutions may be wheeled robot [7], tracked robot [8], legged robot [9] and hybrid ones [10], Among them, wheeled robots are attractive choices because of their simple structure and low energy consumption [11]. However, wheels are unsuitable for crossing obstacles and irregularities, which limits the applications of wheeled robots in unstructured environments [12]. Therefore, researchers have proposed multiple methods to solve the above problems.

The first, passive suspension wheeled robot. A passively-suspended articulated frame could improve the adaptability of wheeled mobile robots for them to work in unstructured environments. Examples of wheeled robots with passively-suspended articulated frames are the rocker-bogie type rovers developed for Mars exploration, e.g., the Perseverance Mars exploration robot [13], the Jade Rabbit 2 lunar exploration robot [14], and the Spirit and Sojourner [15, 16]. The two rocker-bogie mechanisms on each side of the robots maintain all the wheels in contact with the ground, providing high terrain adaptability to the uneven terrain or small obstacles for the robots without any actuation for controlling the internal configuration of the locomotion. Nevertheless, the passively-suspended articulated frames complicate the mechanical structure of a robot and had exhibited limitations in adaptation to a complex terrain with high obstacles and steep slopes [17].

The second, active chassis wheeled robot. Mobile robots with active chassis to control their posture have shown their potential ability to operate in challenging terrains such as high obstacles and steep slopes. These robots include the SRR [18, 19], the Tri-star [20], the Scarab [21] and the passively-actively transformable mobile robot proposed by Jian et al. [22]. Such robots can actively modify their configurations by adjusting their suspension linkages and joints, thereby enhance their stability and traction. Compared to the passively-suspended articulated frame, this kind of locomotion system extends the robot's mobility with simpler mechanical structure, but adds complexity to the control system, and requires extra power resources [23].

The above methods improve the adaptability of the robots to uneven terrain, but the robots still perform poorly in the face of high, steep and vertical obstacles. Wheel-legged hybrid robots caused the researchers' interest because they combine the simple structure and high energy efficiency of the wheeled robots with the adaptability and high obstacle capability of the legged robots [12, 24].

The third, separate wheel-legged robot. These kinds of wheel-legged robots are equipped with separate legs connected to the wheeled robot, such as the Mantis [12], the Wheeleg robot [25], the HyTro robot [26, 27], a hybrid locomotion system proposed by Krovi [28] and a small wheel-legged mobile robot system with two robotic arms proposed by Chang et al. [29]. According to the terrain conditions, the legs and wheels of these robots can be used alternately, which makes the design concepts of these robots simple. This kind of robot is equipped with two different locomotion systems and therefore its mass is high and control system is complex.

The fourth, combined wheel-legged robot. These kinds of wheel-legged mobile robots have wheels attached to their the legs, such as the Hylos [30], the Octopus [31], the ATHLETE [32, 33], the Sherpa [34, 35], the Hybtor [36] and a new mecanum wheel-leg mobile robot proposed by Yun et al. [37]. Such mechanisms allow the robot to actively control the position of the centre of gravity with respect to the contact points with the ground [38, 39]. These robots all have many degrees of freedom which ensures high adaptability to uneven terrain and obstacle-climbing capability. But so many joints

and wheels that need to be actuated independently make the control and locomotion systems very complex.

The fifth, reconfigurable wheel-legged robot. These kinds of wheel-legged mobile robots using reconfigurable modules to achieve wheeled or legged functions. These include the Quattrope robot [40, 41], the FUHAR [42], the TurboQuad [43], the WheeLeR [44], the STEP [45], the mobile robot with retractable leg-wheel modules proposed by Tadakuma et al. [46] and the mobile robot with transformable wheels proposed by Wang et al. [47]. Compared with the robots with separated wheels and legs, this design concept reduces the volume and mass of the robot, but the mechanical design of the reconfigurable modules is relative sophisticated. Such mobile robots may indicate limited carrying capacity and low reliability in dirty environments or in case of shocks, so they are rarely used in practical applications.

The sixth, rotating wheeled leg robot. These kinds of robot locomote with rotating wheeled shape legs or arms, which is a suitable solution for small size robots to reduce the complexity of the control system, while preserving good obstacle climbing ability, such as the Loper [48], RHex [49], and ASGUARD [50]. But robots with rotating legs are constantly subjected to shocks and vibrations in the process of movement, which is not conducive to them to carry mission equipment such as cameras. In particular, the EPI.Q robot [51-53] combines the characters of the rotating legs and the wheels attached to legs. It has four locomotion units each of which contains three wheeled-legs evenly distributed around a carrier. Using planetary gear trains with one input degree of freedom and two output degrees of freedom, the robots can switch from a wheel locomotion to a leg locomotion depending on the dynamic conditions. The legs can rotate independently to climb obstacles, while on flat ground only the wheels are active, which simplifies the control and sensing system of the robots.

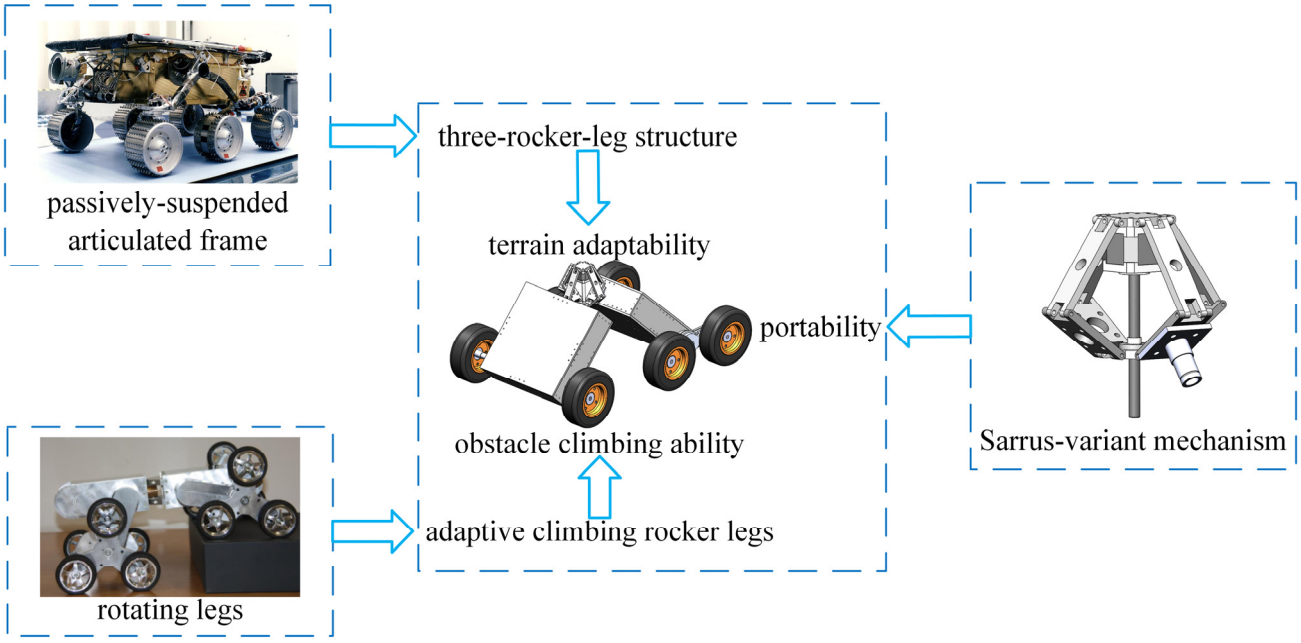

Fig. 1. The superiorities of the proposed robot.

Inspired and different from above research, we propose a portable six-wheeled robot with two adaptive climbing rocker legs and a reconfigurable body, which can reconfigure itself to three different modes, leads to the terrain adaptability, obstacle climbing ability and portability. As shown in Fig. 1, compared with the previous robots, there are three superiorities of the proposed robot. First of all, it

has a simple and compact three-rocker-leg structure, which allows the robot to adapt to the undulation of the terrain and provide a stable platform for task equipment. Secondly, by turning the adaptive climbing rocker legs, it has the capability of adaptive obstacle crossing that does not rely on complex perception and control. And the third, through the Sarrus-variant mechanism, the proposed robot can be folded up for transportation and portability. This robot integrates the advantages of the above robots and overcomes the shortcomings of them, which has a broad application prospect not only in disaster rescue detection, but also in mine clearance and explosive disposal detection.

The rest of the paper is arranged as follows. Section 2 provides the design criteria and mechanical design of a portable six-wheeled mobile robot. Based on the mechanical design, Section 3 presents the geometric constraint, static conditions and motion stability condition for obstacle crossing of the robot. Then, numerical simulation is conducted in Section 4 to validate the theoretical derivations, leading to the parameter identification for the robot in obstacle crossing. A physical prototype of the proposed robot is developed and presented in Section 5, leading to the field experiments that verify the feasibility and manoeuvrability of the proposed mobile robot. Conclusions and future work are addressed in Section 6.

2. Mechanical robot design

In this section, the criteria for designing a portable six-wheeled mobile robot for rescuing purpose is firstly proposed. The detailed mechanical structure design of the proposed mobile robot is then presented.

2.1 Design criteria

The purpose of this study is to develop a small portable self-adaptive obstacle crossing mobile robot that can perform various rescue detection tasks in disastrous fields. The dimension of this robot is about 800 mm × 450 mm × 200 mm. It has a simple mechanical structure and control system for rescuing purpose. The follows are the design criteria:

1) Light weight, the total weight of the robot is less than 10 kg, and some extra weight comes from typically associated detection and rescue devices, such as cameras, microphones, wireless communication devices, and additional task-oriented sensors.

2) High manoeuvrability, the robot can manoeuvre in unstructured environments and can climb vertical obstacles of about 200 mm height; the robot can pivot around a vertical axis on flat grounds to avoid complex manoeuvres with backward motion in a narrow space.

3) Stable motion, the robot has excellent adaptability in unstructured environments characterized by uneven terrain and irregular obstacles, and can maintain the stability of the associated items such as cameras and detection devices.

4) Portability, the robot is portable and can be folded so that it is compact and convenient for transportation (e.g., can be easily carried by a user).

Following these criteria, a reconfigurable wheeled mobile robot is designed as follows.

2.2 Mechanical structure

Based on the design criteria, the mechanical structure of the reconfigurable six-wheeled robot and the three locomotion configurations is illustrated in Fig. 2. As shown in Fig. 2(a), the robot consists of a two-wheeled front body, a Sarrus-variant mechanism and a four-wheeled rear body with two adaptive climbing rocker legs. The front body has two walking wheels driven by two motors independently at

the left and right. The rear body has two adaptive climbing rocker legs symmetrically mounted to itself, and there is an obstacle-crossing wheel on both ends of each rocker leg. The two adaptive climbing rocker legs can passively rotate with respect to the rear body, and the two obstacle-crossing wheels installed on a rocker leg are driven by one DC motor through a series of gears. The front body and the rear body are articulated through a Sarrus-variant mechanism, and there are active pitch motion (achieved through the actuated Sarrrus-variant mechanism) and passive roll motion between them. The eight degrees of freedom of the proposed mobile robot are summarised in Table A1 in the appendix A.

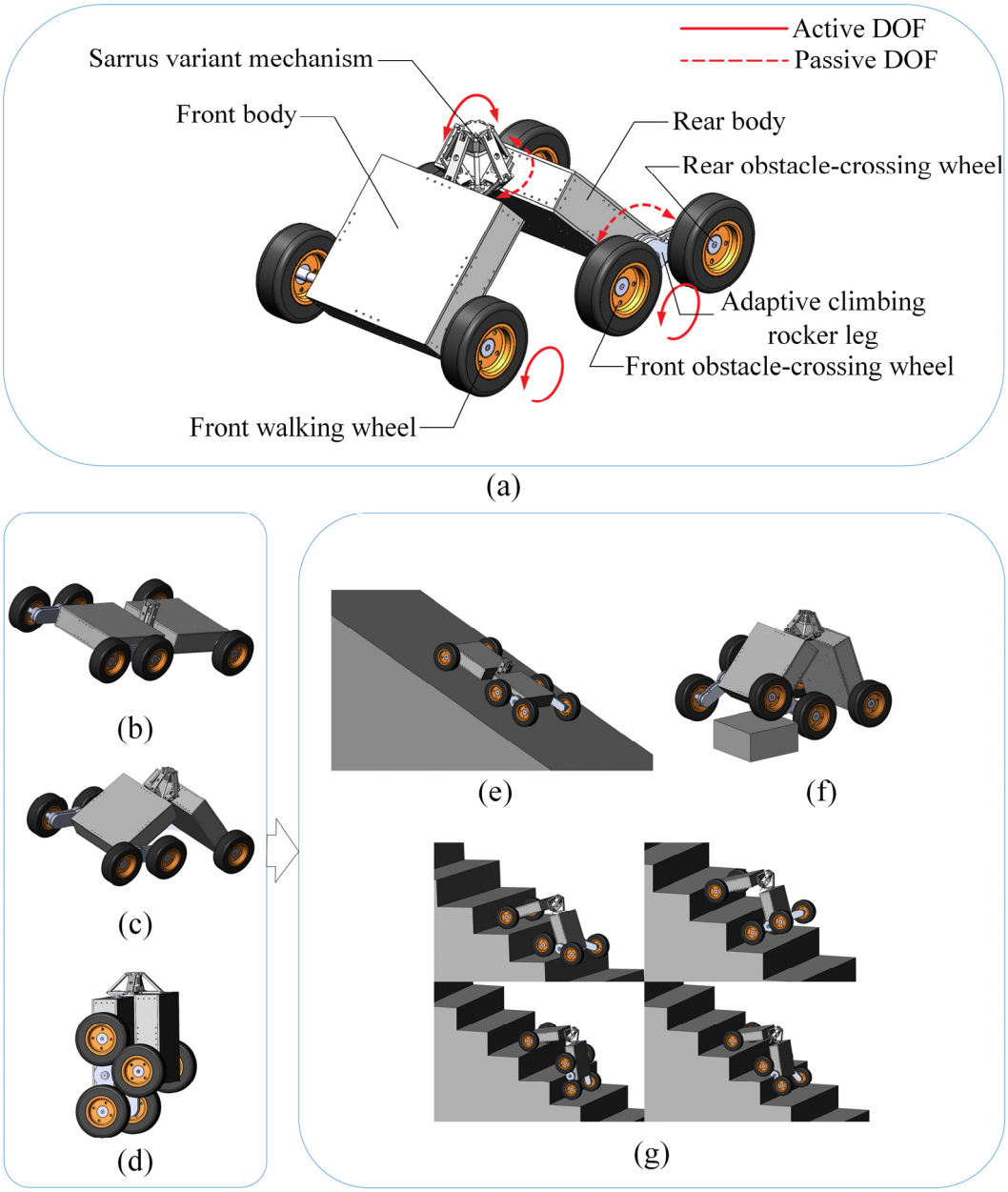

Fig. 2. The mechanical structure of the reconfigurable six-wheeled robot and the three locomotion configurations. a) The mechanical structure of the reconfigurable six-wheeled robot; b) the flat configuration; c) the V-shaped configuration; d) the folded configuration; e) the robot works in the flat configuration to climb a slope; f) the three rocker legs of the robot adapt their configurations relative to the rear body according to the shape of the rough terrain to maintain the contact of the six wheels with the ground and improve the stability of the robot; g) the robot transforms itself into the V-shaped

configuration to raise its centre of gravity and to prevent the chassis from contacting the step edge and climbs stairs by continuously flipping the rocker legs.

The proposed mobile robot can transform itself, through the Sarrus-variant mechanism, into three locomotion configurations as the flat configuration (see Fig. 2(b)), the V-shaped configuration (see Fig. 2(c)), and the folded configuration (see Fig. 2(d)), leads to the terrain adaptability, obstacle climbing ability and portability. When moving on the flat ground or a slope (see Fig. 2(e)), the robot works in the flat configuration to lower its centre of gravity; when working on the rough terrain (see Fig. 2(f)), the front body and the two adaptive climbing rocker legs on both sides form the three rocker legs of the robot, which can adapt their configurations relative to the rear body according to the shape of the rough terrain to maintain the contact of the six wheels with the ground and improve the stability of the robot; when encountering a staircase (see Fig. 2(g)), the robot transforms itself into the V-shaped configuration to raise its centre of gravity and to prevent the chassis from contacting the step edge, it climbs the stairs by continuously flipping the rocker legs; when the robot needs to be carried or transported, it is folded to reduce its size as shown in Fig. 2(d).

2.3 The Sarrus-variant mechanism

Reconfigurability of the robot's locomotion states is implemented by the Sarrus-variant mechanism. As shown in Fig. 3(a), (b) and (c), the Sarrus-variant mechanism with one degree of freedom can convert limited linear motion into circular motion and vice versa [54].

The Sarrus-variant mechanism is constituted of a top plate, a 4-rods upper connecting group, a 4-rods lower connecting group, a bottom plate, a stepping motor, a screw rod, a screw nut and a connecting shaft (see Fig. 3(b)). The top plate, the upper and lower connecting groups and the bottom plate are sequentially linked by three sets of parallel revolute joints. With the stepping motor on the top plate driving the bottom plate through the screw rod and nut, the whole mechanism can achieve a linear reciprocating motion of extension and contraction (see Fig. 3(a) to Fig. 3(c)). As can be seen in Fig. 2(a), the front and rear bodies are connected by the Sarrus-variant mechanism. The front body is fixed on one lower connecting rod of the mechanism through bolts and on the symmetrical side, the rear body is assembled to the mechanism through the connecting shaft. Thus, the front and rear bodies can realize the active relative pitch motion controlled by the stepping motor to reconfigure the robot (see Fig. 3(d)), and the passive relative roll motion to make the robot better adapt to the fluctuations of the terrain (see Fig. 3(e)).

The Sarrus-variant mechanism has two advantages in this design: 1) Self-locking, the mechanism can realize self-locking through the nut and screw. In this way, the robot can maintain the relative configuration of the front and rear bodies without a continuous power supply. 2) Stable, the top plate of the Sarrus-variant mechanism is always parallel to the plane formed by the contact points of the wheels with the ground, which provides a stable platform for locating some mission apparatus such as a camera, as shown in Fig. 3(f).

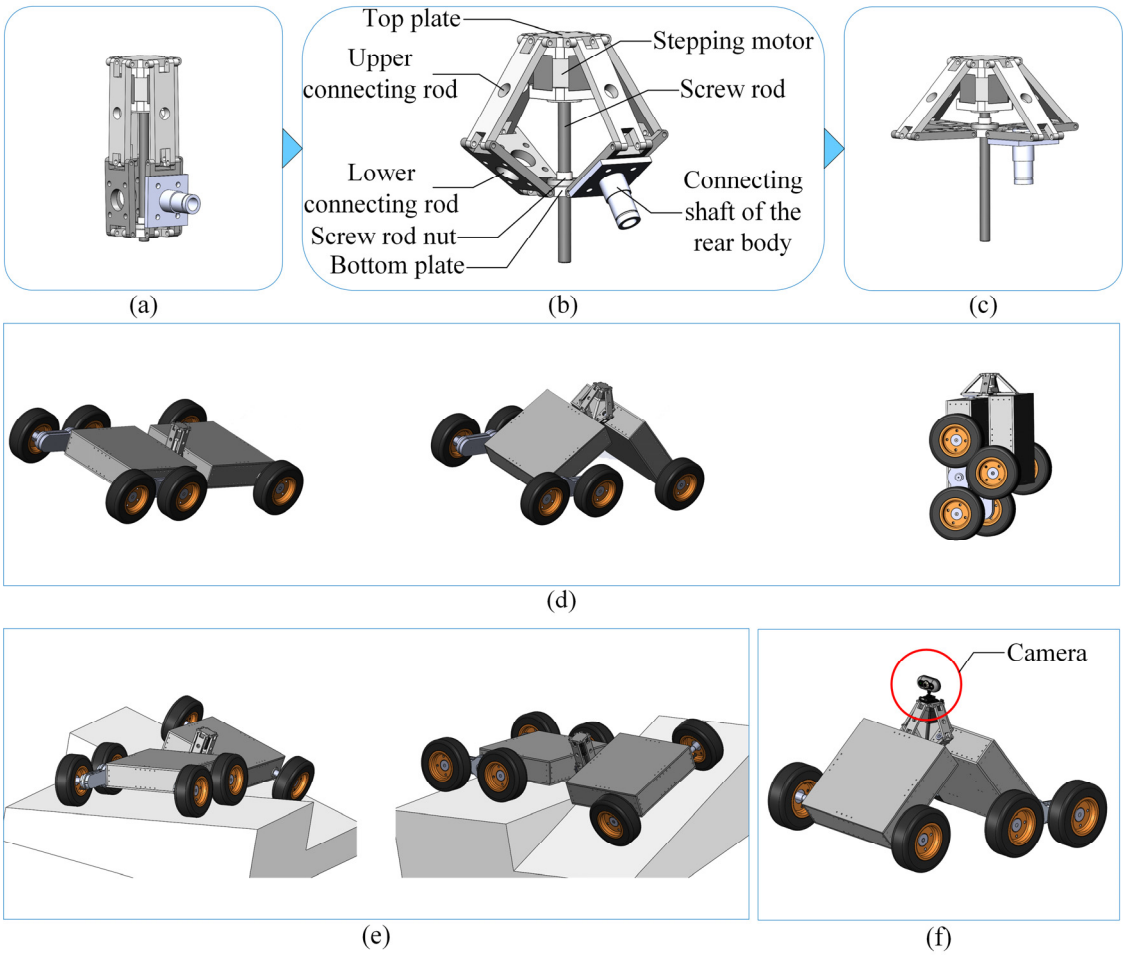

Fig. 3. Mechanical structure and kinematics of the Sarrus-variant mechanism. a) The Sarrus-variant mechanism is in the extended state; b) the structure of the Sarrus-variant mechanism; c) the Sarrus-variant mechanism is in the contraction state; d) the robot's locomotion states are adjusted through the Sarrus-variant mechanism; e) the front body twists to adapt to the fluctuations of the terrain; f) the robot is equipped with a camera.

2.4 The climbing rocker legs

As illustrated in Figs. 4(a) and (b), the adaptive climbing rocker leg and obstacle-crossing wheel system is formed by a parallel-axis gear train connected to a DC motor, a planetary gear train accommodated in the rocker leg (planetary gear frame), and two obstacle-crossing wheels fixed on the wheel shafts on both ends of the rocker leg. The parallel-axis gear train is composed of a motor gear (gear 1 in Fig. 4(b)), a primary gear (dual gear 2 and 2' in Fig. 4(b)) and a secondary gear (gear 3 in Fig. 4(b)). The function of the parallel-axis gear train is to enlarge the output torque of the motor, providing sufficient power for the adaptive climbing rocker leg to overturn and cross obstacles. Therefore, the transmission ratio between the motor gear and the secondary gear, denoted as i_{13}, is set to 5.5. The planetary gear train is composed of a sun gear, a planetary frame, four planetary gears and a wheel shaft on each side. The sun gear 3' in the planetary gear train and the secondary gear 3 in the parallel-axis gear train rotate synchronously and share a central transmission shaft, to transmit the amplified motor output torque to the rocker leg.

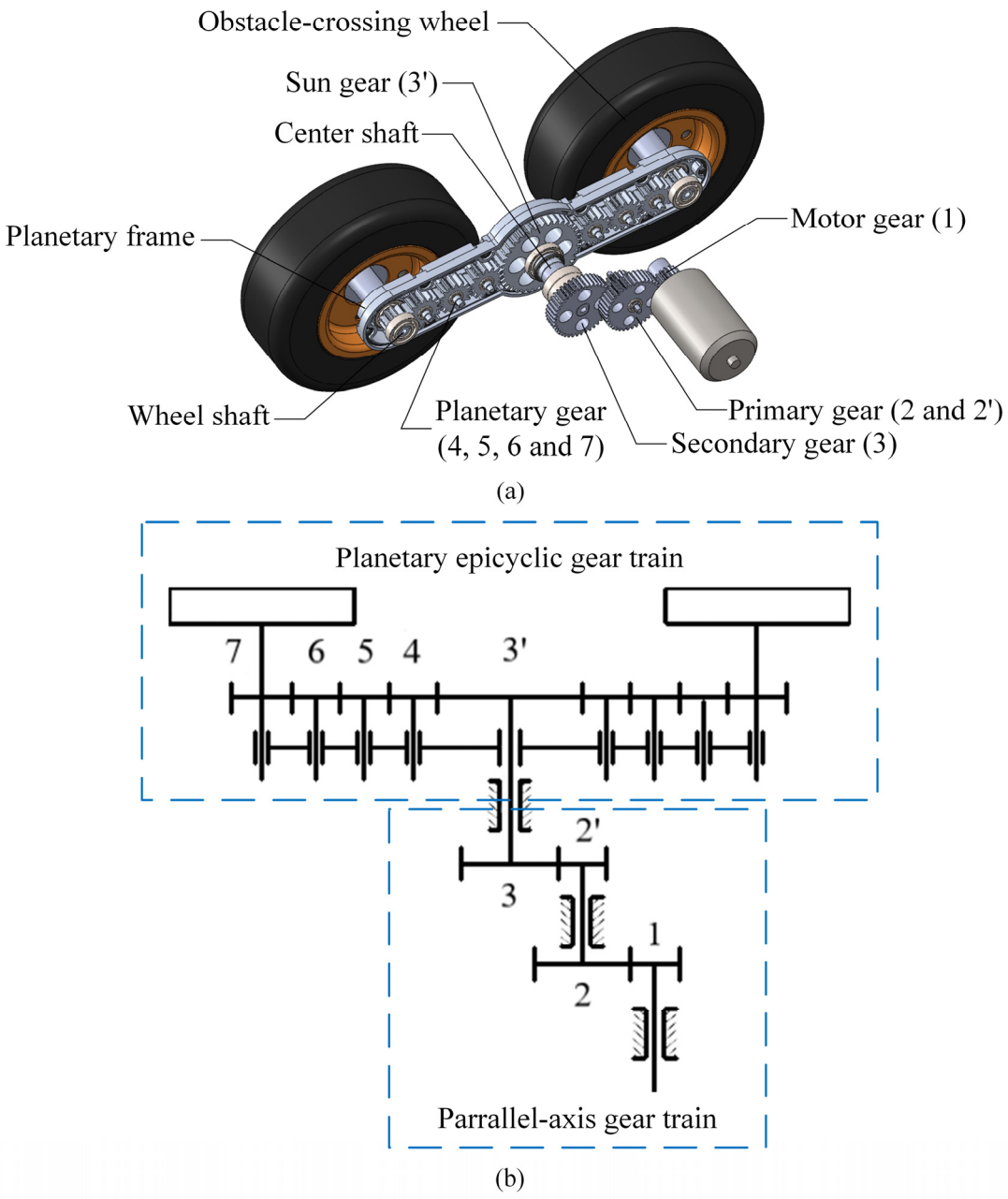

Fig. 4. Structure and transmission of the adaptive climbing rocker leg and obstacle-crossing wheel system. (a) The composition of the adaptive climbing rocker leg; (b) the gear transmission diagram in the climbing rocker leg.

When the robot moves on the smooth-and-even ground, the parallel-axis gear train is maintained as a fixed-axis gear train and the climbing rocker leg will not turn over. The function of the planetary gear train is to increase the speed of the obstacle-crossing wheel, and the transmission ratio between the wheel shaft and the sun gear, denoted as i_{73}, is set to 3.8. Once the obstacle-crossing wheels are blocked by the obstacle, the planetary gear train will be converted into an epicyclic gear train. The amplified motor output torque will be used to drive the adaptive climbing rocker leg to turn around the wheel shaft and prop up the robot.

The number of the planetary gears must be even to guarantee that the rotation direction of the

motor is consistent with that of the wheels, when the rocker legs are locked, and that of the rocker legs, when the wheels are locked, which is necessary for the robot to switch between the wheeled locomotion and legged locomotion without control intervention. Besides, three of the planetary gears (gear 4, 5, and 6 in Fig. 4(b)) are of the same size and designed to be as small as possible to reduce the width of the adaptive climbing rocker leg so as to avoid the contact between the rocker leg and obstacles.

The similar rocker leg principle was used in the design of the EPI.Q robots [51, 52], in which the rocker legs contains three branches with three wheels on each of them. Because the rocker legs containing three branches will make it difficult for the robot to be folded and put into the backpack, which is not convenient for the user to carry. In this design, the bar-shaped rocker leg is adopted to improve the compactness and portability of the robot, even if it sacrifices part of the obstacle crossing capability of the robot.

In this section, the design concept of the robot and the mechanical principle of the Sarrus-variant mechanism and adaptive climbing rocker leg are illustrated in detail. The manoeuvrability of the robot in rugged terrain mainly depends on its obstacle crossing capability. Based on the above design, the kinematics, statics and motion stability of the proposed mobile robot for obstacle crossing are presented in the next section.

3. Modelling

With the Sarrus-variant mechanism and the rocker legs, the robot can cross obstacles of different heights. The obstacle-crossing process of the robot is shown in Fig. 5. It generally takes six steps. After detecting an obstacle, the robot firstly transforms itself into the V-shaped configuration and gets in contact with the obstacle (see Fig. 5(a)). Then, by using the friction between the obstacle and the wheels, the front walking wheels pull the front body of the robot to climb over the obstacle (see Fig. 5(b)). After this, the robot continues to move forward (see Fig. 5(c)) until the front obstacle-crossing wheels are in contact with the obstacle. Subsequently, with the walking wheels moving forward, the adaptive climbing rocker legs on both sides of the robot turn over, lifting the rear body of the robot (see Fig. 5(d)). When the rear obstacle-crossing wheels contact the edge of the obstacle (see Fig. 5(e)), the robot climbs the obstacle with all the six wheels, leading to the stage that the whole robot comes over the obstacle (see Fig. 5(f)).

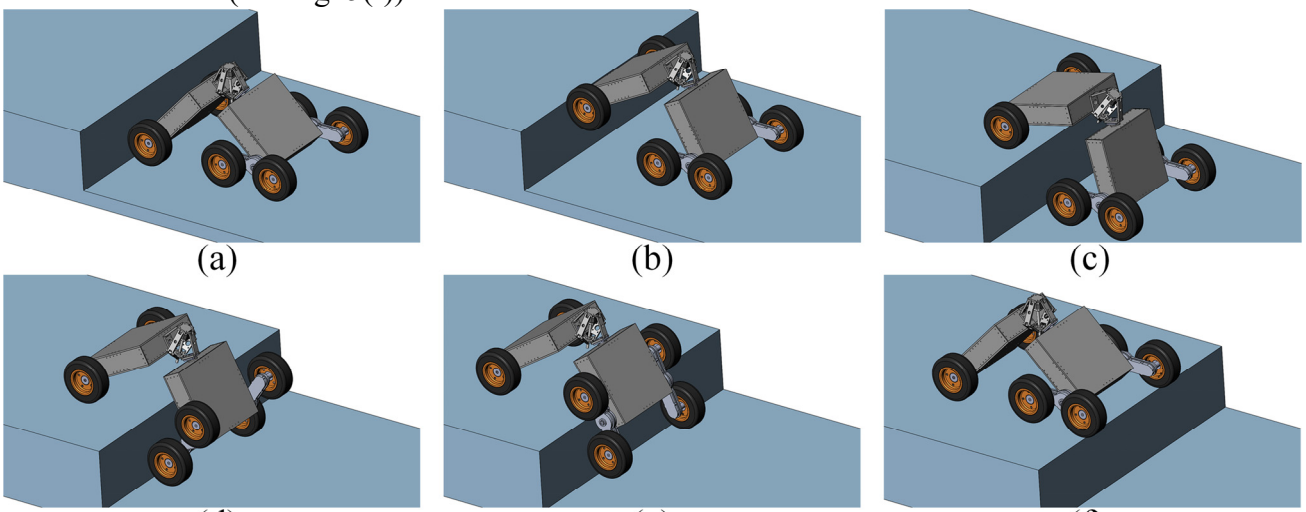

Fig. 5. The obstacle crossing process of the robot. a) The robot firstly transforms itself into the V-shaped configuration and gets in contact with the obstacle after detecting an obstacle; b) the front walking wheels pull the robot's front body to climb over the obstacle by using the friction between the obstacle and the wheels; c) the robot continues to move forward until the front obstacle-crossing wheels are in contact with the obstacle; d) the climbing rocker legs on both sides turn over and lift the rear body of the robot with the walking wheels moving forward; e) the rear obstacle-crossing wheels contact the edge of the obstacle; f) the robot climbs the obstacle with all the six wheels.

Based on the mechanical design of the robot presented in Section 2 and the obstacle-crossing process described above, it can be found that whether the robot can climb and cross an obstacle is related to the configuration between the front and rear bodies which is determined by the Sarrus-variant mechanism. To climb obstacles, the robot must satisfy the conditions of geometric passing capability, static passing capability and motion stability, simultaneously. For geometric passing capability, the robot cannot interfere or collide with obstacles in the process of obstacle crossing. For static passing capability, the front walking wheels must be able to pull the front body along the vertical surface of the obstacle, and the climbing rocker legs must be capable of supporting the rear body through overturning. In terms of motion stability, it requires that the robot maintains balance during the whole obstacle-crossing process. In order to find the relation between the configurations of the Sarrus-variant mechanism and the obstacle crossing capability of the proposed robot, in this section, the geometry and position analysis of the robot, and geometric constraint, static conditions and motion stability condition for obstacle crossing are formulated and analysed.

3.1. Geometry and position analysis of the six-wheeled robot

To better analyse the obstacle crossing performance of the robot, the geometric model of the robot is established in this section. The main geometrical parameters of the robot are shown in Fig. 6. In the model, the coordinate frame $O_0\{X_0, Y_0, Z_0\}$ is a fixed inertia frame, $O_1\{X_1, Y_1, Z_1\}$ is a body coordinate frame located at the intersection of the centre line of the robot's rear body and the rotation axes of the rocker legs on both sides, $O_2\{X_2, Y_2, Z_2\}$ is a body coordinate frame located at the centre point of the left adaptive climbing rocker leg, $O_3\{X_3, Y_3, Z_3\}$ is a body coordinate frame located at the centre point of the right adaptive climbing rocker leg, and $O_4\{X_4, Y_4, Z_4\}$ is a body coordinate frame located at the articulation of the front and rear body (with the axis Y_4 coincides with the central axis of the rear body and the central axis of the front body is always in the X_4 - Y_4 plane). In addition, the structure and geometric parameters of the robot are defined as shown in the figure. Where B is the length between two wheels in the width direction (which is approximately the same as the width of the front and rear bodies), l_b is the length of the front and rear bodies, l_e is the length of the adaptive climbing rocker leg, r is the radius of the wheels (all the wheels are of the same dimension), θ_l and θ_r are respectively the swing angles of the left and right adaptive climbing rocker legs. δ is the rotation angle of the rear body with respect to the coordinate frame $O_1\{X_1, Y_1, Z_1\}$ in the X_1 - Y_1 plane, which is treated as the variant angle of the robot. θ_f is the rotation angle of the coordinate frame $O_4\{X_4, Y_4, Z_4\}$ with respect to the coordinate frame $O_1\{X_1, Y_1, Z_1\}$ in the X_4 - Z_4 plane. The structure parameters are collected in a vector as $[r \quad l_b \quad l_e \quad B]^T$, and the geometric variables are collected in a vector as $[\theta_l \quad \theta_r \quad \theta_f \quad \delta]^T$.

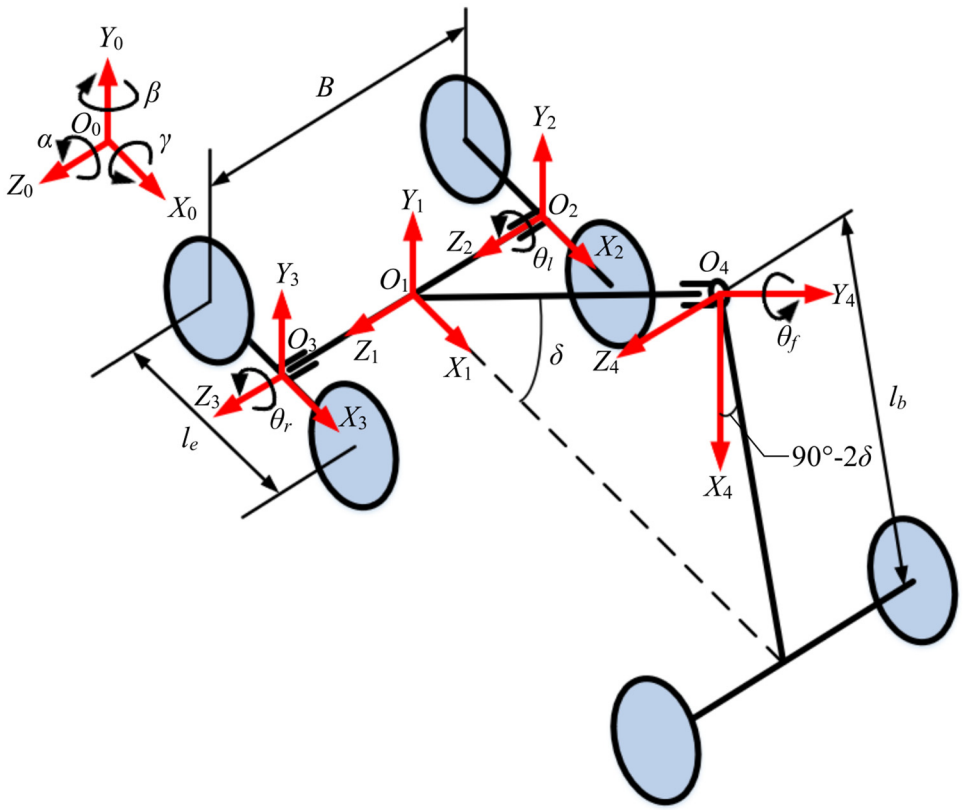

Fig. 6. Schematic diagram and geometrical parameters of the robot.

Referring to Fig. 6, the rotation matrix of the robot coordinate frame $O_1\{X_1, Y_1, Z_1\}$ relative to the fixed coordinate frame $O_0\{X_0, Y_0, Z_0\}$ is [55]:

$$\begin{aligned}\mathbf{R}(\beta,\alpha,\gamma) &= Rot(y,\beta)\,Rot(z,\alpha)\,Rot(x,\gamma)\\ &= \begin{bmatrix} \mathrm{c}\alpha\mathrm{c}\beta & \mathrm{s}\beta\mathrm{s}\gamma-\mathrm{c}\beta\mathrm{c}\gamma\mathrm{s}\alpha & \mathrm{c}\gamma\mathrm{s}\beta+\mathrm{c}\beta\mathrm{s}\alpha\mathrm{s}\gamma \\ \mathrm{s}\alpha & \mathrm{c}\alpha\mathrm{c}\gamma & -\mathrm{c}\alpha\mathrm{s}\gamma \\ -\mathrm{c}\alpha\mathrm{s}\beta & \mathrm{c}\beta\mathrm{s}\gamma+\mathrm{c}\gamma\mathrm{s}\beta\mathrm{s}\alpha & \mathrm{c}\beta\mathrm{c}\gamma-\mathrm{s}\beta\mathrm{s}\alpha\mathrm{s}\gamma \end{bmatrix}\end{aligned} \tag{1}$$

In Eq. (1), α, β, γ are, respectively, the pitch angle, steer angle and roll angle of the robot. These angles can be detected with the gyroscopic sensors attached to the robot. In the equation, c stands for the cosine function and s stands for the sine function, the same notations are used for the rest of the equations.

Let the coordinates of the origin O_1 expressed in the fixed coordinate frame be (a, b, c). The transformation matrix of the robot coordinate frame $O_1\{X_1, Y_1, Z_1\}$ relative to the fixed coordinate frame $O_0\{X_0, Y_0, Z_0\}$ can be obtained in the homogeneous transformation matrix form as

$${}^{0}\mathbf{T}_{1} = \begin{bmatrix} \mathrm{c}\alpha\mathrm{c}\beta & \mathrm{s}\beta\mathrm{s}\gamma-\mathrm{c}\beta\mathrm{c}\gamma\mathrm{s}\alpha & \mathrm{c}\gamma\mathrm{s}\beta+\mathrm{c}\beta\mathrm{s}\alpha\mathrm{s}\gamma & a \\ \mathrm{s}\alpha & \mathrm{c}\alpha\mathrm{c}\gamma & -\mathrm{c}\alpha\mathrm{s}\gamma & b \\ -\mathrm{c}\alpha\mathrm{s}\beta & \mathrm{c}\beta\mathrm{s}\gamma+\mathrm{c}\gamma\mathrm{s}\beta\mathrm{s}\alpha & \mathrm{c}\beta\mathrm{c}\gamma-\mathrm{s}\beta\mathrm{s}\alpha\mathrm{s}\gamma & c \\ 0 & 0 & 0 & 1 \end{bmatrix} \tag{2}$$

Further, referring to Fig. 6, the transformation matrix of the two adaptive climbing rocker legs and the front body with respect to the robot coordinate frame $O_1\{X_1, Y_1, Z_1\}$ can be written as

$$
{}^{1}\mathbf{T}_{2}=\begin{bmatrix} \mathrm{c}\theta_{l} & -\mathrm{s}\theta_{l} & 0 & 0 \\ \mathrm{s}\theta_{l} & \mathrm{c}\theta_{l} & 0 & 0 \\ 0 & 0 & 1 & -B/2 \\ 0 & 0 & 0 & 1 \end{bmatrix} \tag{3}
$$

for the left adaptive climbing rocker leg,

$$
{}^{1}\mathbf{T}_{3}=\begin{bmatrix} \mathrm{c}\theta_{r} & -\mathrm{s}\theta_{r} & 0 & 0 \\ \mathrm{s}\theta_{r} & \mathrm{c}\theta_{r} & 0 & 0 \\ 0 & 0 & 1 & B/2 \\ 0 & 0 & 0 & 1 \end{bmatrix} \tag{4}
$$

for the right adaptive climbing rocker leg, and

$$
\begin{aligned}
{}^{1}\mathbf{T}_{4} &= \begin{bmatrix} \mathrm{s}\delta & \mathrm{c}\delta & 0 & l_{b}\mathrm{c}\delta \\ -\mathrm{c}\delta & \mathrm{s}\delta & 0 & l_{b}\mathrm{s}\delta \\ 0 & 0 & 1 & 0 \\ 0 & 0 & 0 & 1 \end{bmatrix} \begin{bmatrix} \mathrm{c}\theta_{f} & 0 & \mathrm{s}\theta_{f} & 0 \\ 0 & 1 & 0 & 0 \\ -\mathrm{s}\theta_{f} & 0 & \mathrm{c}\theta_{f} & 0 \\ 0 & 0 & 0 & 1 \end{bmatrix} \\
&= \begin{bmatrix} \mathrm{s}\delta\mathrm{c}\theta_{f} & \mathrm{c}\delta & \mathrm{s}\delta\mathrm{s}\theta_{f} & l_{b}\mathrm{c}\delta \\ -\mathrm{c}\delta\mathrm{c}\theta_{f} & \mathrm{s}\delta & -\mathrm{c}\delta\mathrm{s}\theta_{f} & l_{b}\mathrm{s}\delta \\ -\mathrm{s}\theta_{f} & 0 & \mathrm{c}\theta_{f} & 0 \\ 0 & 0 & 0 & 1 \end{bmatrix}
\end{aligned} \tag{5}
$$

for the front body.

For the convenience of analysis, assuming the centroid of each part of the robot is at its geometric centre, the expression of the centre of mass (CoM) of the robot in the robot coordinate frame $O_1\{X_1, Y_1, Z_1\}$ is as follows:

$$
{}^{1}\boldsymbol{P}_{1}=\frac{m_{fb}{}^{1}\boldsymbol{p}_{fb}+m_{rb}{}^{1}\boldsymbol{p}_{rb}+m_{w}{}^{1}\boldsymbol{p}_{lw}+m_{w}{}^{1}\boldsymbol{p}_{rw}+m_{a}{}^{1}\boldsymbol{p}_{2}+m_{a}{}^{1}\boldsymbol{p}_{3}}{m} \tag{6}
$$

In equation Eq. (6), m_{fb}, m_{rb}, m_w and m_a represent the mass of the front body, the mass of the rear body, the mass of the front walking wheel, and the mass of the adaptive climbing rocker leg, respectively (note that the mass of the Saruss-viriant mechanism is omitted since it is much lighter than the other components). m represents the overall mass of the robot and $m = m_{fb} + m_{rb} + 2m_w + 2m_a$; ${}^{1}\boldsymbol{p}_{fb}$, ${}^{1}\boldsymbol{p}_{rb}$, ${}^{1}\boldsymbol{p}_{lw}$, ${}^{1}\boldsymbol{p}_{rw}$, ${}^{1}\boldsymbol{p}_{2}$ and ${}^{1}\boldsymbol{p}_{3}$ are, respectively, the vectors of the centroids of the front body, the rear body, the front walking wheels and the adaptive climbing rocker legs on both sides expressed in the robot coordinate frame $O_1\{X_1, Y_1, Z_1\}$. Referring to Fig. 6, these vectors can be found as

$$
{}^{1}\boldsymbol{p}_{fb}=\begin{bmatrix} \frac{l_{b}\mathrm{s}2\delta\mathrm{s}\delta\mathrm{c}\theta_{f}}{2}+\frac{l_{b}\mathrm{c}2\delta\mathrm{c}\delta}{2}+l_{b}\mathrm{c}\delta \\ -\frac{l_{b}\mathrm{s}2\delta\mathrm{c}\delta\mathrm{c}\theta_{f}}{2}+\frac{l_{b}\mathrm{c}2\delta\mathrm{s}\delta}{2}+l_{b}\mathrm{s}\delta \\ -\frac{l_{b}\mathrm{s}2\delta\mathrm{s}\theta_{f}}{2} \\ 1 \end{bmatrix} \tag{7}
$$

$$ {}^{1}\boldsymbol{p}_{rb} = \begin{bmatrix} \frac{l_b \,\mathrm{c}\delta}{2} & \frac{l_b \,\mathrm{s}\delta}{2} & 0 & 1 \end{bmatrix}^T \tag{8} $$

$$ {}^{1}\boldsymbol{p}_{lw} = \begin{bmatrix} l_b \,\mathrm{s}2\delta \,\mathrm{s}\delta \,\mathrm{c}\theta_f + l_b \,\mathrm{c}2\delta \,\mathrm{c}\delta - \frac{B \,\mathrm{s}\delta \,\mathrm{s}\theta_f}{2} + l_b \,\mathrm{c}\delta \\ -l_b \,\mathrm{s}2\delta \,\mathrm{c}\delta \,\mathrm{c}\theta_f + l_b \,\mathrm{c}2\delta \,\mathrm{s}\delta + \frac{B \,\mathrm{c}\delta \,\mathrm{s}\theta_f}{2} + l_b \,\mathrm{s}\delta \\ -l_b \,\mathrm{s}2\delta \,\mathrm{s}\theta_f - \frac{B \,\mathrm{c}\theta_f}{2} \\ 1 \end{bmatrix} \tag{9} $$

$$ {}^{1}\boldsymbol{p}_{rw} = \begin{bmatrix} l_b \,\mathrm{s}2\delta \,\mathrm{s}\delta \,\mathrm{c}\theta_f + l_b \,\mathrm{c}2\delta \,\mathrm{c}\delta + \frac{B \,\mathrm{s}\delta \,\mathrm{s}\theta_f}{2} + l_b \,\mathrm{c}\delta \\ -l_b \,\mathrm{s}2\delta \,\mathrm{c}\delta \,\mathrm{c}\theta_f + l_b \,\mathrm{c}2\delta \,\mathrm{s}\delta - \frac{B \,\mathrm{c}\delta \,\mathrm{s}\theta_f}{2} + l_b \,\mathrm{s}\delta \\ -l_b \,\mathrm{s}2\delta \,\mathrm{s}\theta_f + \frac{B \,\mathrm{c}\theta_f}{2} \\ 1 \end{bmatrix} \tag{10} $$

$$ {}^{1}\boldsymbol{p}_2 = \begin{bmatrix} 0 & 0 & -B/2 & 1 \end{bmatrix}^T \tag{11} $$

$$ {}^{1}\boldsymbol{p}_3 = \begin{bmatrix} 0 & 0 & B/2 & 1 \end{bmatrix}^T \tag{12} $$

In this paper, we focus on the bilateral obstacle crossing motion of the robot, hence it is assumed that the central line of the robot is always in the X_1 - Y_1 plane. Under such assumption, the angle θ_f is constant and it has $\theta_f = 0$.

Then, by substituting Eqs. (7) throughout (12) into Eq. (6), the vector of the CoM of the robot with respect to the robot coordinate frame $O_1\{X_1, Y_1, Z_1\}$ can be obtained as

$$ {}^{1}\boldsymbol{P}_1 = \begin{bmatrix} \frac{M_1 l_b \cos\delta}{2m} & \frac{M_2 l_b \sin\delta}{2m} & 0 & 1 \end{bmatrix}^T \tag{13} $$

with $M_1 = 3m_{fb} + m_{rb} + 8m_w$ and $M_2 = m_{fb} + m_{rb}$.

In the process of obstacle crossing, the change of the robot's pitch angle α is much greater than the roll angle γ and the steering angle β. By omitting the roll angle γ and the steer angle β, the robot's centre of mass coordinate expressed in the fixed coordinate frame $O_0\{X_0, Y_0, Z_0\}$ is

$$ {}^{0}\boldsymbol{P}_1 = {}^{0}\mathbf{T}_1 \, {}^{1}\boldsymbol{P}_1 = \begin{bmatrix} \frac{M_1 l_b \cos\alpha \cos\delta}{2m} - \frac{M_2 l_b \sin\alpha \sin\delta}{2m} + a \\ \frac{M_2 l_b \cos\alpha \sin\delta}{2m} + \frac{M_1 l_b \sin\alpha \cos\delta}{2m} + b \\ c \\ 1 \end{bmatrix} \tag{14} $$

After obtaining the CoM of the robot, its obstacle crossing performance can be analysed from the following three aspects.

3.2. Geometric constraint for obstacle crossing

When the robot climbs over the obstacle, it is configured to avoid the contact between the robot body and the obstacle before the rear obstacle-crossing wheels touching the obstacle. Even if contact occurs, it should have a mechanism of disengagement, so that the robot has a good geometric passing capability. During the obstacle-crossing process, the robot is most likely to contact the obstacle in the obstacle-crossing phase (e) (See Fig. 5(e)), which needs to be avoided and the geometric constraint for obstacle crossing in this phase is analysed as follows.

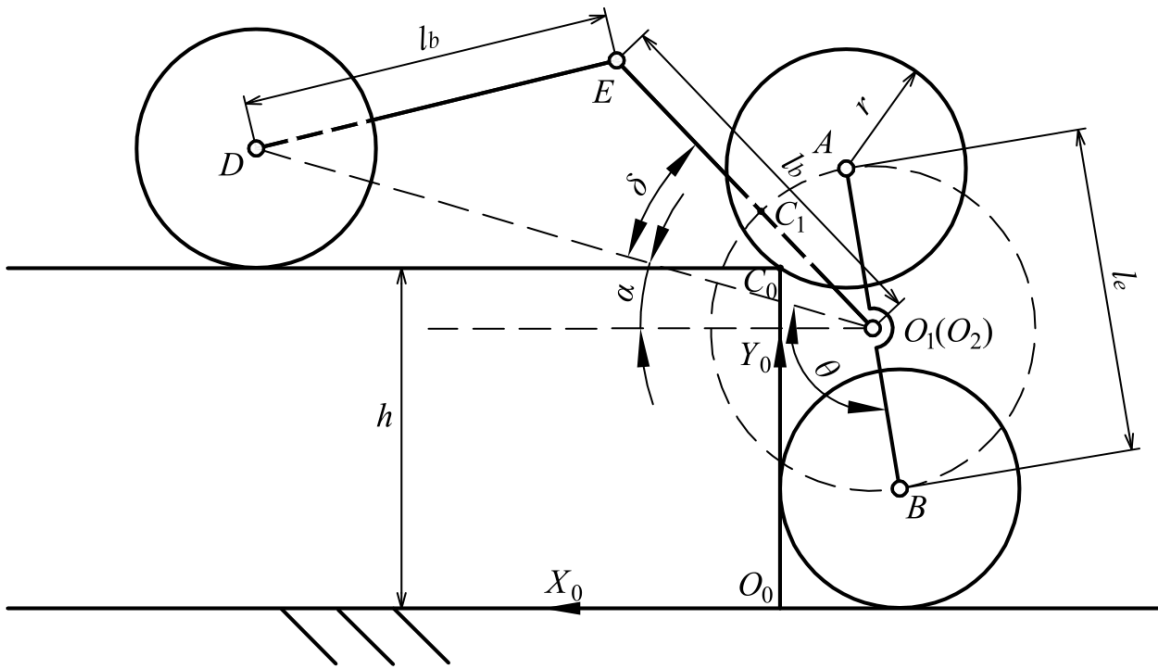

Fig. 7. Geometry for the critical state of the robot obstacle crossing process.

Figure 7 shows the configuration of the robot obstacle crossing in phase (e) at the critical state. At this stage, after the front obstacle-crossing wheels hitting the wall of the obstacle, the adaptive climbing rocker legs turn over and put the rear obstacle-crossing wheels in contact with the edge of the obstacle. By omitting the steering angle of the robot, the swing angles of the adaptive climbing rocker legs on both sides are the same, that is $\theta_l = \theta_r = \theta$. In this configuration, both the rear obstacle-crossing wheels and the front obstacle-crossing wheels are in contact with the obstacle.

At this critical position of obstacle crossing, the contact point between the rear obstacle-crossing wheel and the edge of the obstacle is set as C_0. Referring to Fig. 7, point C_1 is the intersection of the robot rear body and the circle centering at the centre point O_1 of the adaptive climbing rocker leg, with its diameter being the length of the adaptive climbing rocker leg l_e. According to the geometric relationship between the robot and the obstacle, there exists the relation that

$$\frac{l_e}{2}\sin\left(A_1 + A_2\right) + 2l_b\cos\delta\sin\alpha = h \tag{15}$$

with $A_1 = \arccos\dfrac{\left(h-r\right)^2 + l_e^{\,2}}{2l_e\sqrt{\left(h-r\right)^2 + r^2}}$ and $A_2 = \arccos\dfrac{r}{\sqrt{\left(h-r\right)^2 + r^2}}$. Where h is the height of the obstacle, l_b is the length of the front and rear bodies, l_e is the length of the climbing rocker leg, r is the radius of the wheels, α is the pitch angle of the robot, δ is the rotation angle of the rear body with

respect to the coordinate frame $O_1\{X_1, Y_1, Z_1\}$ in the X_1 - Y_1 plane.

In order to ensure that the robot's rear body will not interfere with the edge of the obstacle when the robot's rocker legs are overturned, and the rear obstacle-crossing wheels can climb on the top surface of the obstacle, the coordinate ${}^0y_{C1}$ of point C_1 must be greater than the coordinate ${}^0y_{C0}$ of point C_0, that is

$$ {}^0y_{C_1} > {}^0y_{C_0} \tag{16}$$

where,

$$\begin{cases} {}^0y_{C_1} = r\sin\delta\cos\alpha + r\cos\delta\sin\alpha + h - 2l_b\cos\delta\sin\alpha + r \\ {}^0y_{C_0} = h \end{cases} \tag{17}$$

Substituting Eq. (17) into Eq. (16), the geometric constraint for obstacle crossing of the proposed robot can be expressed as,

$$ r\sin\delta\cos\alpha + r\cos\delta\sin\alpha + h - 2l_b\cos\delta\sin\alpha + r > h \tag{18}$$

Eq. (18) can further be expressed as a function with respect to δ as

$$ G(\delta) = r\sin\delta\cos\alpha + r\cos\delta\sin\alpha - 2l_b\cos\delta\sin\alpha + r > 0 \tag{19}$$

in which, it has

$$ \sin\alpha = \frac{h - \frac{l_e}{2}\sin(A_1 + A_2)}{2l_b\cos\delta} \tag{20}$$

and

$$ \cos\alpha = \sqrt{1 - (\sin\alpha)^2} \tag{21}$$

From the above derivation, it can be seen that when $G(\delta) > 0$, the proposed robot satisfies the geometric constraint for obstacle crossing, which is defined as the geometric passing capability.

3.3 Static conditions for obstacle crossing

In addition to the geometric constrain derived in the previous section, the robot must also satisfy certain static conditions. Referring to the obstacle crossing process presented in Fig. 5, in phase (a), the robot must be able to lift its front body along the vertical surface of the obstacle. In phase (c), the adaptive climbing rocker legs must be capable of propping up the rear body by turning over. Hence, the static analysis must be conducted to find the conditions that must be satisfied for obstacle-crossing of the robot.

Figure 8 shows the geometric and force parameters of the robot in the obstacle-crossing phase (a). In this phase, the front walking wheels are in contact with the obstacle, the friction force f_1 between the wheels and the obstacle gradually lifts the front walking wheels. The four obstacle-crossing wheels keep moving forwards, on one hand maintaining the contact between the front walking wheels and the obstacle, and on the other hand leading to the generation of a torque T that helps the lifting action. In order to cross the obstacle, the robot must be able to complete lifting the front walking wheels on the top of the obstacle to get into phase (c). Hence, in this phase, the static condition for lifting the front walking wheels must be satisfied.

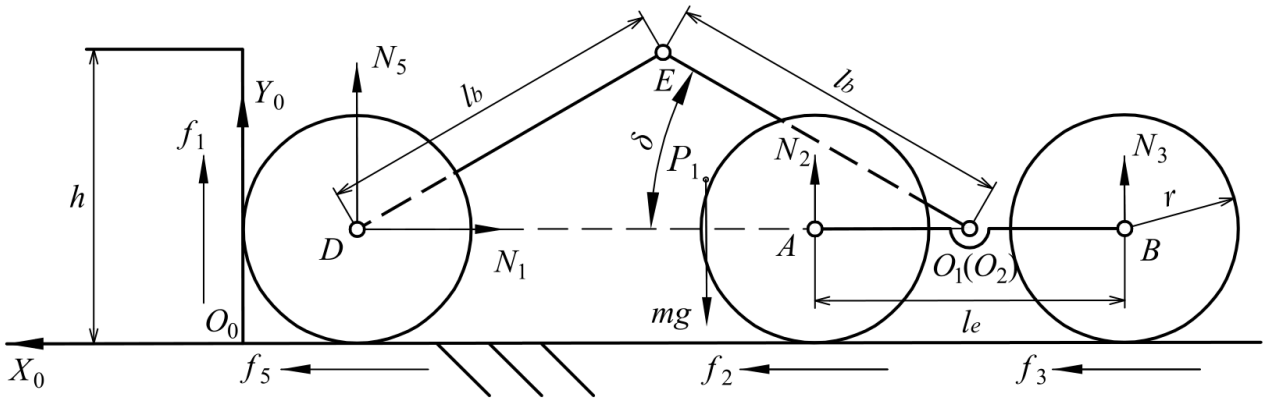

Fig. 8. The static forces of the robot in the obstacle-crossing phase (a).

Referring to Fig. 8, in phase (a), the equilibrium equations of the system can be derived as follows

$$\begin{cases} N_1 = f_2 + f_3 + f_5 \\ f_1 + N_2 + N_3 + N_5 = mg \\ \dfrac{N_2 l_e}{2} + A_3 + A_4 + 2N_5 l_b \cos\delta + f_5 r = \dfrac{M_1 g l_b \cos\delta}{2} + \dfrac{N_3 l_e}{2} \end{cases} \tag{22}$$

where $A_3 = (f_2 + f_3)r$, $A_4 = f_1(r + 2l_b\cos\delta)$, N_1 is the normal force between the front walking wheels and the obstacle, N_2, N_3, and N_5 are respectively the normal forces between the ground and the front and rear obstacle-crossing wheels, and the front walking wheels, f_1 is the friction force between the obstacle and the front walking wheels, and f_2, f_3, and f_5 are the friction forces between the ground and the front and rear obstacle-crossing wheels, and the front walking wheels, respectively. The mass and geometric parameters are the same as those presented in Sections 3.1 and 3.2. The first and second lines of Eq. (22) represent static equilibrium equations of the robot in the horizontal and vertical directions, respectively. The third line represents the torque equilibrium equation of the robot about point $O_1(O_2)$.

Further, referring to Fig. 4(b), the static equilibrium condition of the adaptive climbing rocker legs in the obstacle-crossing phase (a) is shown in Fig. 9.

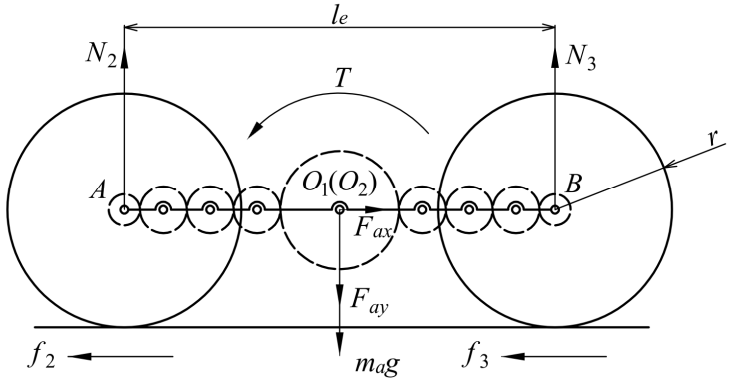

Fig. 9. The static condition of the adaptive climbing rocker legs in the obstacle-crossing phase (a).

In Fig. 9, F_{ax} and F_{ay} are the normal forces between the adaptive climbing rocker legs and the rear body of the robot in the horizontal and vertical directions, respectively. T represents the output torque of the adaptive climbing rocker legs' central gear shafts, which is applied to the sun gear 3. Referring to Fig. 9 and Fig. 4(b), the torque equilibrium equations of the adaptive climbing rocker legs can be derived as follows

$$\begin{cases} \dfrac{N_2 l_e}{2} + (f_2 + f_3) r = T + \dfrac{N_3 l_e}{2} \\ (f_2 + f_3) r i_{73} = T \end{cases} \tag{23}$$

where i_{73} is the transmission ratio between the obstacle-crossing wheel shaft and the sun gear. The first line represents the torque equilibrium equation of the adaptive climbing rocker legs about point $O_1(O_2)$. The second line represents the proportional relationship between the friction torques of the two obstacle-crossing wheels and the output torque T of the adaptive climbing rocker legs' central gear shafts.

In order to simplify the analysis, it is assumed that the sliding friction coefficient between the wheels and the ground and the obstacle surface is μ. If the front walking wheels can also lift the robot's front body under the condition of sliding friction, the front body can also be lifted when the pressure on the front walking wheels is large enough and the front walking wheels are subjected to static friction or rolling friction. Therefore, it is assumed that the robot's front walking wheels rotate relative to the obstacle's vertical surface and the ground, and the friction forces on the front walking wheels are $f_1 = \mu N_1$ and $f_5 = \mu N_5$.

When the robot is on the point of lifting the front body, the front walking wheels will be off the ground. Hence there are $N_5 = 0$ and $f_5 = 0$. Substituting the conditions $f_1 = \mu N_1$, $N_5 = 0$ and $f_5 = 0$ into Eqs. (22) and (23), the normal force N_3 between the ground and the rear obstacle-crossing wheels can be obtained as

$$N_3 = \frac{mg}{2} + \left(\frac{r}{l_e} - \frac{\mu}{2} - \frac{r i_{73}}{l_e} \right) \frac{M_1 g l_b \cos\delta}{2\left(r i_{73} + \mu \left(r + 2 l_b \cos\delta \right) \right)} \tag{24}$$

Only when the front walking wheels are off the ground, in such case the normal force N_3 is still greater than 0, can it indicate that the robot can lift the front body. Otherwise, the adaptive climbing rocker legs will turn over, and the robot will not be able to lift the front body.

According to Eq. (24) and the above derivation, the static condition for the proposed robot to lift the front body in phase (a) can be expressed as a function with respect to δ as

$$F_1(\delta) = \frac{mg}{2} + \left(\frac{r}{l_e} - \frac{\mu}{2} - \frac{r i_{73}}{l_e} \right) \frac{M_1 g l_b \cos\delta}{2\left(r i_{73} + \mu \left(r + 2 l_b \cos\delta \right) \right)} > 0 \tag{25}$$

After the front body climbs over the obstacle, the robot will continue to move forward until the front obstacle-crossing wheels are in contact with the obstacle and get into the obstacle-crossing phase (c). Figure 10 shows the geometric and force parameters of the robot in the obstacle-crossing phase (c). In this phase, the front walking wheels move forward on the top of the obstacle and pull the robot forward by the friction force f_1. The front obstacle-crossing wheels are in contact with the vertical surface of the obstacle and locked by the friction forces f_2 and f_4. The adaptive climbing rocker legs gradually turn over and prop up the rear body of the robot. To cross the obstacle, the robot must be able to support itself by turning the adaptive climbing rocker legs to get into phase (e). Hence, in this

phase, static condition for propping up the rear body must be satisfied.

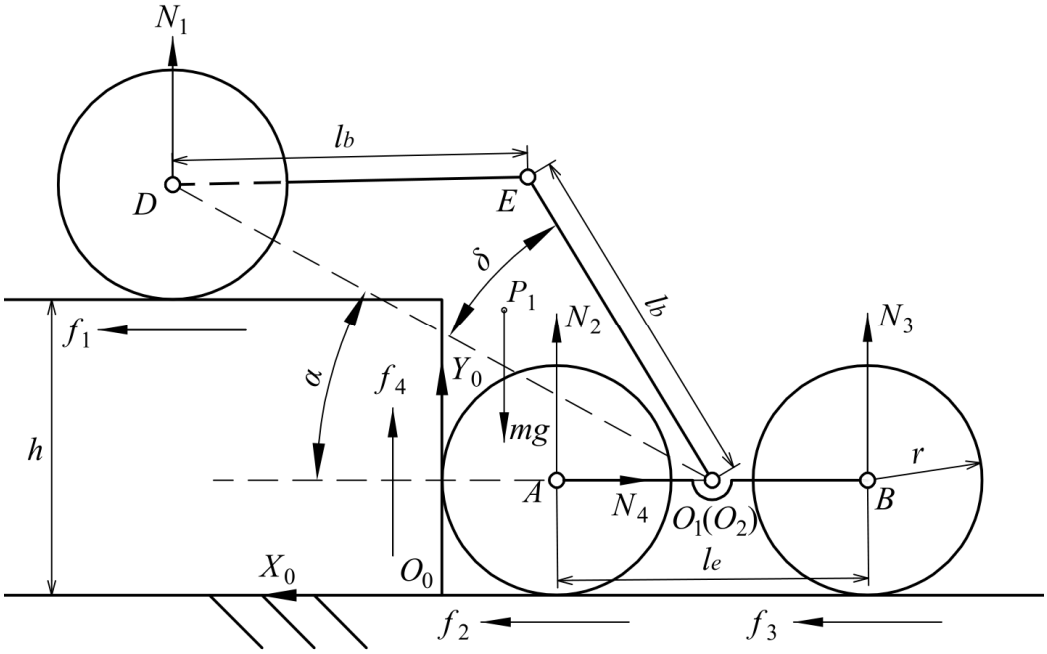

Fig. 10. The static forces of the robot in the obstacle-crossing phase (c).

Referring to Fig. 10, in phase (c), the equilibrium equations of the system can be derived as follows

$$\begin{cases} N_4 = f_1 + f_2 + f_3 \\ f_4 + N_1 + N_2 + N_3 = mg \\ \dfrac{N_2 l_e}{2} + f_4\left(\dfrac{l_e}{2} + r\right) + A_3 + A_5 \\ \quad = A_6 + A_7 - A_8 + \dfrac{N_3 l_e}{2} \end{cases} \tag{26}$$

where $A_5 = 2N_1 l_b \cos\delta\cos\alpha$, $A_6 = f_1\left(2l_b \cos\delta \sin\alpha - r\right)$, $A_7 = \dfrac{M_1 g l_b \cos\delta\cos\alpha}{2}$, $A_8 = \dfrac{M_2 g l_b \sin\delta\sin\alpha}{2}$, N_4 is the normal force between the front obstacle-crossing wheels and the obstacle, f_4 is the friction force between the front obstacle-crossing wheels and the obstacle. The other geometric and force parameters are the same as those in Eq. (22). In this configuration, the pitch angle α of the robot can be derived from Fig. 10 as

$$\begin{cases} \sin\alpha = \dfrac{h}{2l_b \cos\delta} \\ \cos\alpha = \sqrt{1 - \left(\dfrac{h}{2l_b \cos\delta}\right)^2} \end{cases} \tag{27}$$

In addition, referring to Fig. 4(b), the static condition of the adaptive climbing rocker legs in the obstacle-crossing phase (c) is shown in Fig. 11.

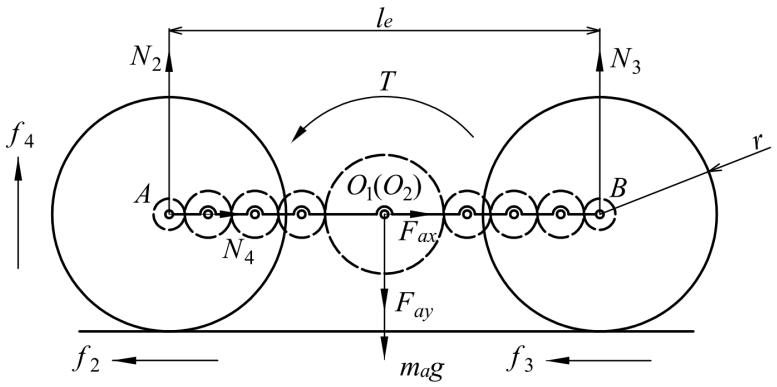

Fig. 11. The static condition of the adaptive climbing rocker legs in the obstacle-crossing phase (c).

The geometric and force parameters are the same as those in Eq. (23). Referring to Fig. 11 and Fig. 4(b), the torque equilibrium equations of the adaptive climbing rocker legs can be derived as

$$\begin{cases} \dfrac{N_2 l_e}{2} + f_4\left(\dfrac{l_e}{2}+r\right) + A_3 = T + \dfrac{N_3 l_e}{2} \\ \left(f_2+f_3+f_4\right) r i_{73} = T \end{cases} \tag{28}$$

To simplify the analysis, it is assumed that the output torques of the robot's front motors are large enough to make the front walking wheels rotate relative to the top surface of the obstacle. The front walking wheels are subject to sliding friction, which is $f_1 = \mu N_1$.

When the adaptive climbing rocker legs are about to turn over, the rear obstacle-crossing wheels will be off the ground. Hence there are $N_3 = 0$ and $f_3 = 0$.

Substituting $f_1 = \mu N_1$, $N_3 = 0$, $f_3 = 0$ and Eq. (27) into Eq. (26) and Eq. (28), the normal force N_1 between the top surface of obstacle and the front walking wheels can be obtained as

$$N_1 = \frac{\dfrac{mgl_e}{2\left(1-1/i_{73}\right)} - \dfrac{M_1 g A_9}{2} + \dfrac{M_2 gh\sin\delta}{4\cos\delta}}{\dfrac{l_e}{2\left(1-1/i_{73}\right)} + \mu\left(h-r\right) - 2A_9} \tag{29}$$

where $A_9 = \sqrt{\left(l_b\cos\delta\right)^2 - \left(\dfrac{h}{2}\right)^2}$.

Only when the adaptive climbing rocker legs turn over and the rear obstacle-crossing wheels are off the ground, in such case the normal force N_1 is still greater than 0, can it indicate that the robot can prop up itself in the obstacle-crossing phase (c). Otherwise, the robot will overturn.

According to Eq. (29) and the above derivation, the static condition for the proposed robot to prop up itself by turning the adaptive climbing rocker legs in phase (c) can further be expressed as a function with respect to δ as

$$F_2\left(\delta\right) = \frac{\dfrac{mgl_e}{2\left(1-1/i_{73}\right)} - \dfrac{M_1 g A_9}{2} + \dfrac{M_2 gh\sin\delta}{4\cos\delta}}{\dfrac{l_e}{2\left(1-1/i_{73}\right)} + \mu\left(h-r\right) - 2A_9} > 0 \tag{30}$$

From the above derivations, it can be seen that when $F_1(\delta) > 0$ and $F_2(\delta) > 0$, the proposed robot satisfies the static conditions for obstacle crossing, which are defined as the static passing capability.

3.4 Motion stability condition for obstacle crossing

Besides the geometric constraint and static conditions, the robot must keep motion stability during the obstacle-crossing process. Referring to the obstacle-crossing process presented in Fig. 5, we can find that in phase (d), the robot is most prone to overturn, which is the worst case and needs to be avoided. We assume that if the robot can keep motion stability for this phase, it can maintain stability for the other phases. In this section, the static stability margin (SSM) [36] is used to investigate the motion stability of the robot in obstacle-crossing process.

Figure 12 shows the geometry of the robot in the obstacle-crossing phase (d). In this phase, the robot keeps turning the adaptive climbing rocker legs and props up itself with the front walking wheels moving forward.

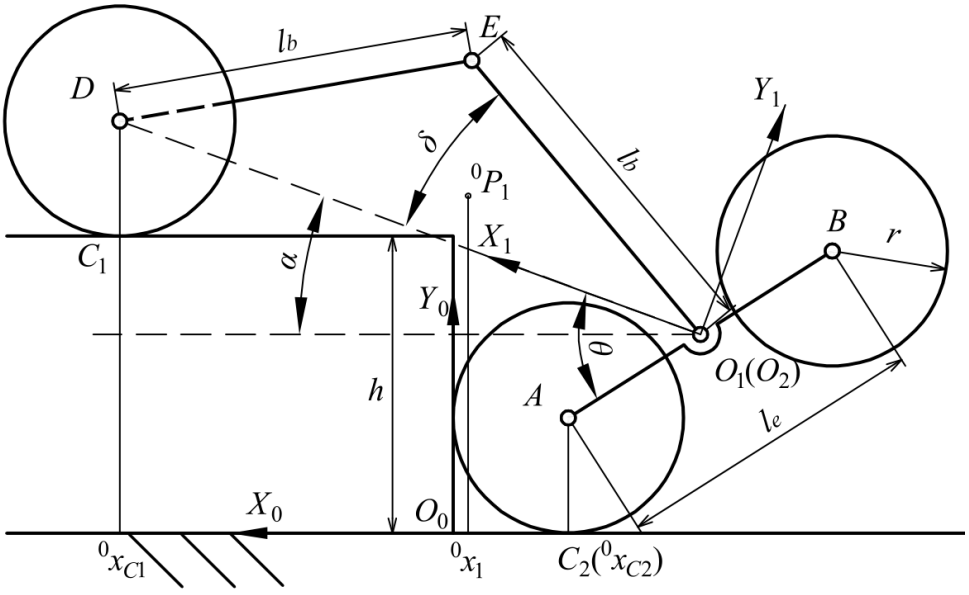

Fig. 12. The geometry of the robot in the obstacle-crossing phase (d).

The static stability margin (SSM) for a given support polygon is defined as the smallest of the distances from the centre of mass projection to the edges of the support polygon, and the static stability condition is SSM > 0 [56]. In phase (d), the stability condition of the robot is secured if the projection of COM of the robot (${}^0P_1$) on the X_0-axis, ${}^0x_1$, lies between the x coordinates of contact points (C_1 and C_2) of the front walking wheels, ${}^0x_{C1}$, and the front obstacle-crossing wheels, ${}^0x_{C2}$, with the top surface of the obstacle and the ground, that is:

$$ {}^0x_{C_2} < {}^0x_1 < {}^0x_{C_1} \tag{31} $$

According to the geometric relationship between the robot and the obstacle shown in Fig. 12, there are

$$ {}^0x_1 = \frac{A_7}{mg} - \frac{A_8}{mg} - A_{10} - r \tag{32} $$

$$ {}^0x_{C_1} = 2l_b \cos\delta \cos\alpha - A_{10} - r \tag{33} $$

$$^{0}x_{C_2} = -r \tag{34}$$

where $A_{10} = \sqrt{\frac{l_e^{\,2}}{4} - \left(h - 2l_b \cos\delta \sin\alpha\right)^2}$.

And there exits the relation that

$$h - 2l_b \cos\delta \sin\alpha = l_e \sin\left(\theta - \alpha\right) \tag{35}$$

In the above equations, the geometric parameters are the same as those in Sections 3.1 and 3.2.

By substituting Eqs. (32) throughout (34) into Eq. (31), the following two functions are formulated

$$S_1(\alpha) = {}^{0}x_{C_1} - {}^{0}x_1 = 2l_b \cos\delta \cos\alpha - \frac{A_7}{mg} + \frac{A_8}{mg} \tag{36}$$

$$S_2(\alpha) = {}^{0}x_1 - {}^{0}x_{C_2} = \frac{A_7}{mg} - \frac{A_8}{mg} - A_{10} \tag{37}$$

According to Eq. (31), $S_1(\alpha) > 0$ and $S_2(\alpha) > 0$ are the static stability conditions for the proposed robot to prop up itself.

Equation (36) can be further rearranged as

$$S_1(\alpha) = \left(1 - \frac{M_1}{4m}\right) 2l_b \cos\delta \cos\alpha + \frac{M_2 l_b \sin\delta \sin\alpha}{2m} \tag{38}$$

In the obstacle-crossing phase (d), the range of α is

$$\arcsin\left(\frac{h - \frac{l_e}{2}}{2l_b \cos\delta}\right) \le \alpha \le \arcsin\left(\frac{h}{2l_b \cos\delta}\right) \tag{39}$$

Therefore, there exists $\sin(\alpha) > 0$ and $\cos(\alpha) > 0$.

In addition, in Eq. (38), $\frac{M_1}{4m}$ is always less than 1, and the range of δ is 0~90°, which means that $\sin(\delta) > 0$ and $\cos(\delta) > 0$. Hence $S_1(\alpha)$ is always greater than 0. And as long as $S_2(\alpha)$ is greater than 0, the robot satisfied the static stability condition.

Further, the differentiation of Eq. (37) with respect to α can be obtained as

$$S_2'(\alpha) = -\frac{M_1 l_b \cos\delta \sin\alpha}{2m} - \frac{M_2 l_b \sin\delta \cos\alpha}{2m} - \frac{\left(h - 2l_b \cos\delta \sin\alpha\right) 2l_b \cos\delta \cos\alpha}{\sqrt{\frac{l_e^{\,2}}{4} - \left(h - 2l_b \cos\delta \sin\alpha\right)^2}} \tag{40}$$

In phase (d), $(\theta - \alpha)$ is always greater than 0. According to Eq. (35), it can be seen that $(h - 2l_b \cos\delta \sin\alpha)$ is always greater than 0. In addition, there are $\sin(\alpha) > 0$, $\cos(\alpha) > 0$, $\sin(\delta) > 0$ and $\cos(\delta) > 0$. Hence $S_2'(\alpha)$ is always less than 0 in phase (d), which means that when α reaches the maximum value, the minimum value of $S_2(\alpha)$ can be obtained.

Substituting $\alpha_{\max} = \arcsin\left(\frac{h}{2l_b\cos\delta}\right)$ into Eq. (37), it yields

$$S_2(\alpha_{\max}) = \frac{M_1\sqrt{(2l_b\cos\delta)^2 - h^2}}{4m} - \frac{M_2 h\sin\delta}{4m\cos\delta} - \frac{l_e}{2} \tag{41}$$

As long as $S_2(\alpha_{\max})$ is greater than 0, $S_2(\alpha)$ is always greater than 0 and the robot satisfies the stability condition.

From the above derivation, the stability condition for obstacle crossing of the proposed robot can be expressed as a further function with respect to δ as

$$S(\delta) = \frac{M_1\sqrt{(2l_b\cos\delta)^2 - h^2}}{4m} - \frac{M_2 h\sin\delta}{4m\cos\delta} - \frac{l_e}{2} > 0 \tag{42}$$

From the above derivation, it can be seen that when $S(\delta) > 0$, the proposed robot satisfies the stability condition for obstacle crossing, which are defined as the motion stability.

Hence, in this section, with respect to the variant angle δ, the geometric constraint, static conditions and motion stability condition for obstacle crossing of the proposed mobile robot are derived and formulated in functions as $G(\delta) > 0$, $F_1(\delta) > 0$, $F_2(\delta) > 0$, and $S(\delta) > 0$. As long as these equations are satisfied, the geometric passing capability, static passing capability, and motion stability of the robot for obstacle crossing are secured. In the next section, numerical simulation is used to simulate the above derivations and to identify feasible parameters for prototype development.

4. Numerical simulation and parametric study

In the previous section, we established the geometric constraint $G(\delta)$, static conditions $F_1(\delta)$, $F_2(\delta)$ and stability condition $S(\delta)$ for obstacle crossing of the proposed robot. In this section, numerical simulation is conducted to find appropriate parameters for prototype development.

It can be seen that the obstacle crossing capability of the six-wheeled robot is closely related to the robot's variant angle δ and the friction coefficient μ. The static condition $F_1(\delta)$ is only related to the friction coefficient between the wheel and the ground and obstacle surface. The static condition $F_2(\delta)$ is related to the friction coefficient and the obstacle height. And the geometric constraint $G(\delta)$ and stability condition $S(\delta)$ are only related to the obstacle height. Only when $G(\delta) > 0$, $F_1(\delta) > 0$, $F_2(\delta) > 0$ and $S(\delta) > 0$ are satisfied simultaneously, the robot can cross the obstacle of height h. Based on this, we can control the variant angle δ of the robot to realize obstacle crossing at different height and under different friction conditions.

In this section, we will solve the feasible region of the variant angle δ that the robot can climb over obstacles of different heights and friction coefficients through numerical simulation. In this simulation, the parameters are assigned as: the robot's front body mass m_{fb} = 3.6 kg, rear body mass m_{rb} = 2 kg, front and rear body length l_b = 240 mm, walking wheel mass m_w = 0.55 kg and radius r = 77.5 mm, adaptive climbing rocker leg length l_e = 210 mm and mass m_a = 1.6 kg. By substituting the parameters into the equations $G(\delta) = 0$, $F_1(\delta) = 0$, $F_2(\delta) = 0$ and $S(\delta) = 0$, and solving the implicit functions of the equations about variant angle δ and obstacle crossing height h or friction coefficient μ by using MATLAB®, we can get the curves of the limit value of h or μ as a function of δ. And then the feasible region of δ can be obtained. According to the parameters given above, numerical

simulations are presented in this section as follows.

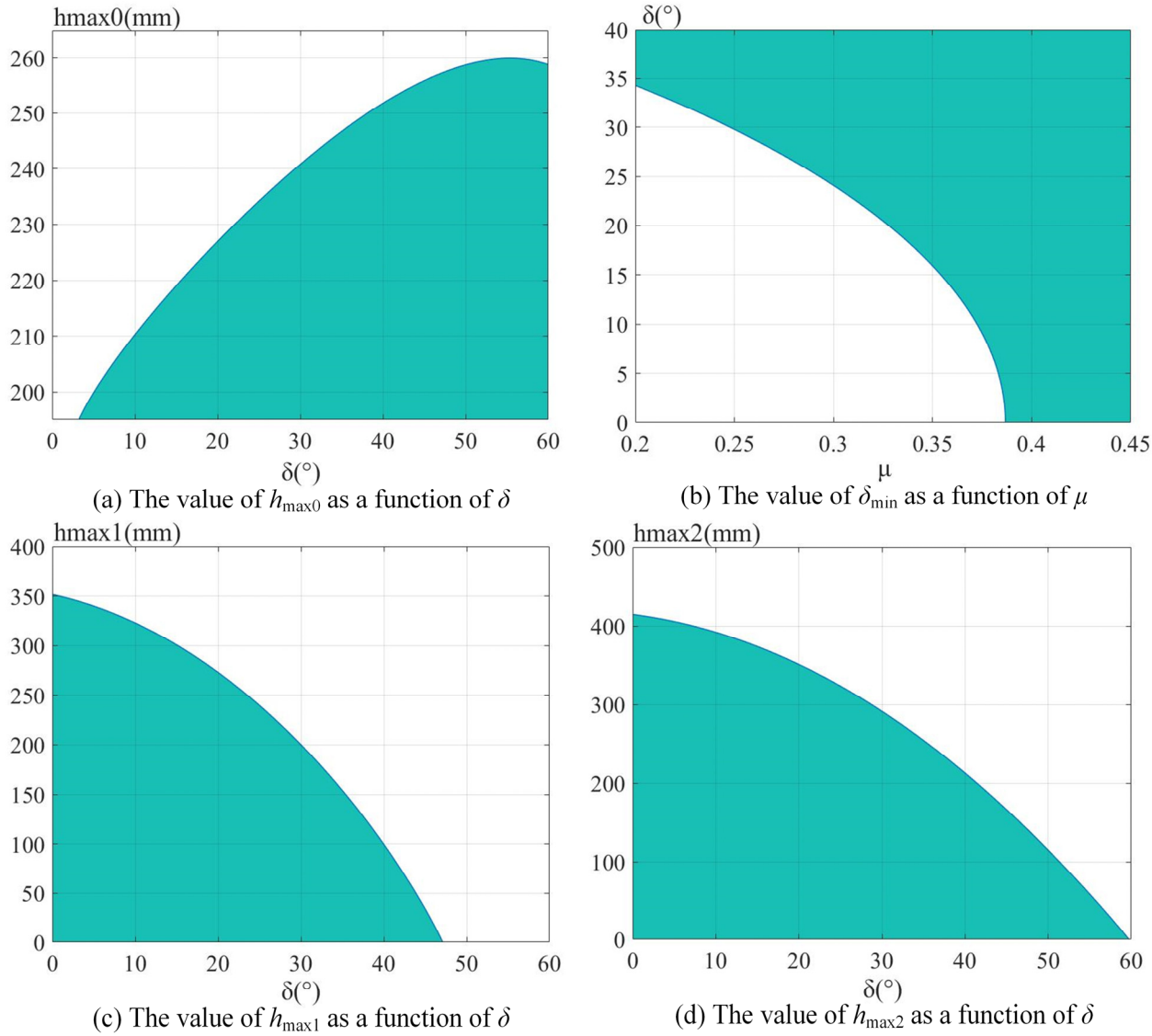

Fig. 13. The feasible regions of the variant angle δ of the robot.

4.1 Numerical simulation for geometric passing capability

According to Eq. (19), when $G(\delta) = 0$, h reaches the maximum obstacle crossing height, denoted as h_{max0}, of the robot satisfying geometric constraint at the current variant angle δ. Solving the implicit function given as $G(\delta) = 0$ by using MATLAB®, the curve of h_{max0} as a function of δ can be obtained and illustrated in Fig. 13(a). The shadowed part in the figure is the feasible region of δ where the robot satisfies the geometric constraint $G(\delta) > 0$. It can be seen from the results that due to the limitation of the robot geometric size, when the height of the obstacle is lower than 195 mm, the robot does not need to be variant and has the geometric passing capability, while when the height of the obstacle is higher than 260 mm, the robot cannot cross the obstacle; when the height of the obstacle is greater than 195 mm, with the increase of h, the robot must increase the variant angle δ correspondingly to have the geometric passing capability for the obstacle.

4.2 Numerical simulation for static passing capability

According to Eq. (25), when $F_1(\delta) = 0$, δ reaches the minimum variant angle, denoted as δ_{min}, at

which the robot can lift the front body in the obstacle-crossing phase (b) under the current friction coefficient μ. Solving the implicit function given as $F_1(\delta) = 0$ with MATLAB®, the curve of δ_{min} changing with respect to μ can be computed and indicated in Fig. 13(b). The shadowed region in Fig. 13(b) is the feasible region of δ where the robot satisfies the static condition $F_1(\delta) > 0$. It can be seen from the results that with the decrease of friction coefficient μ, the robot needs to increase the variant angle δ correspondingly to lift the front body in the obstacle-crossing phase (b). When the friction coefficient $\mu > 0.38$, the robot can lift the front body in the obstacle-crossing phase (b) without changing the variant angle δ.

Further, according to Eq. (30), when $F_2(\delta) = 0$, h reaches the maximum obstacle crossing height, denoted as h_{max1}, that the robot can prop up itself by turning the adaptive climbing rocker legs under the current variant angle δ and friction coefficient μ. In order to ensure that the obstacle-crossing wheels do not slip when crossing the obstacle, $\mu = 0.4$ is selected. Solving the implicit function given as $F_2(\delta) = 0$ by using MATLAB®, the curve of h_{max1} changing with respect to δ is obtained and shown in Fig. 13(c). The shadowed part in Fig. 13(c) is the feasible region of δ where the robot satisfies the static condition $F_2(\delta) > 0$. It can be seen from the results that when the height of the obstacle is higher than 350 mm, the robot cannot cross the obstacle, and with the increase of h, the robot must decrease the variant angle δ correspondingly to have the static passing capability for the obstacle.

4.3 Numerical simulation for motion stability

According to Eq. (42), when $S(\delta) = 0$, h reaches the maximum obstacle crossing height, denoted as h_{max2}, of the robot satisfying the motion stability condition under the current variant angle δ. Similarly, solving the implicit function given as $S(\delta) = 0$ by using MATLAB®, the curve of h_{max2} as a function of δ is obtained and illustrated in Fig. 13(d). The shadowed part in Fig. 13(d) is the feasible region of δ where the robot satisfies the motion stability condition $S(\delta) > 0$. It can be seen from the figure that with the increase of h, the robot must decrease the variant angle δ correspondingly to have the motion stability for the obstacle. And at the same variant angle δ, the maximum obstacle height h_{max1} satisfying the static condition is less than the maximum obstacle height h_{max2} satisfying the static stability condition, which means that when the static condition $F_2(\delta) > 0$ is satisfied, the stability condition $S(\delta) > 0$ must also be satisfied.

In this section, the feasible region of the variant angle δ that the robot can climb over when facing obstacles of different heights has been obtained through numerical simulation. The simulation results show that the robot can satisfy the design criteria of climbing over 200 mm vertical obstacles under the given geometric parameters. In the next section, a prototype is developed based on the given geometric parameters, and a series of experiments are carried out to prove the correctness of the simulation results.

5. Prototype development and field experiments

Based on the design, obstacle crossing analysis and numerical simulation presented in the previous sections, in this section a physical prototype of the proposed mobile robot is developed, and by using it, field experiments are carried out to verify the proposed design and validate the theoretical derivations.

5.1. Basic specifications of the prototype

Based on the mechanical design and theoretical analysis presented above, a physical prototype of the proposed robot was developed as shown in Fig. 14. The prototype can be transformed into three locomotion configurations as discussed in Section 2, i.e. the V-shaped configuration in Fig. 14(a), the

flat configuration in Fig. 14(b) and the folded configuration in Fig. 14(c). In the folded configuration, the prototype can be tied with a rope and carried on the back by the operator, which means the robot satisfies the portable design criteria.

The structure parameters and technical specifications of the prototype are listed in Table 1. The robot's overall dimensions are 780 mm (length) × 454 mm (width) × 190 mm (height). The overall mass is 9.9 kg, including a 24 V lithium battery to power the whole robot. The robot is driven by four DC motors and has position and velocity control.

Table 1 Structure parameters and technical specifications of the prototype

Structure parameters			
Parameter	**Value**	**Parameter**	**Value**
m_{fb}	3.6 kg	l_b	240 mm
m_{rb}	2 kg	l_e	210 mm
m_w	0.55 kg	R	77.5 mm
m_a	1.6 kg	B	400 mm
Technical specifications			
Parameter	**Value**	**Parameter**	**Value**
Maximum speed (tile floor)	0.5 m/s	Maximum obstacle crossing height	210 mm (μ = 0.4)
Motors	4 DC motors 1 stepping motor	Communication range	200 mm (open area)
Battery	Lithium rechargeable	Battery weight	910 g
Wheel controllers	Velocity control	Steering controllers	Position control
Camera	Yes	GPS	Yes

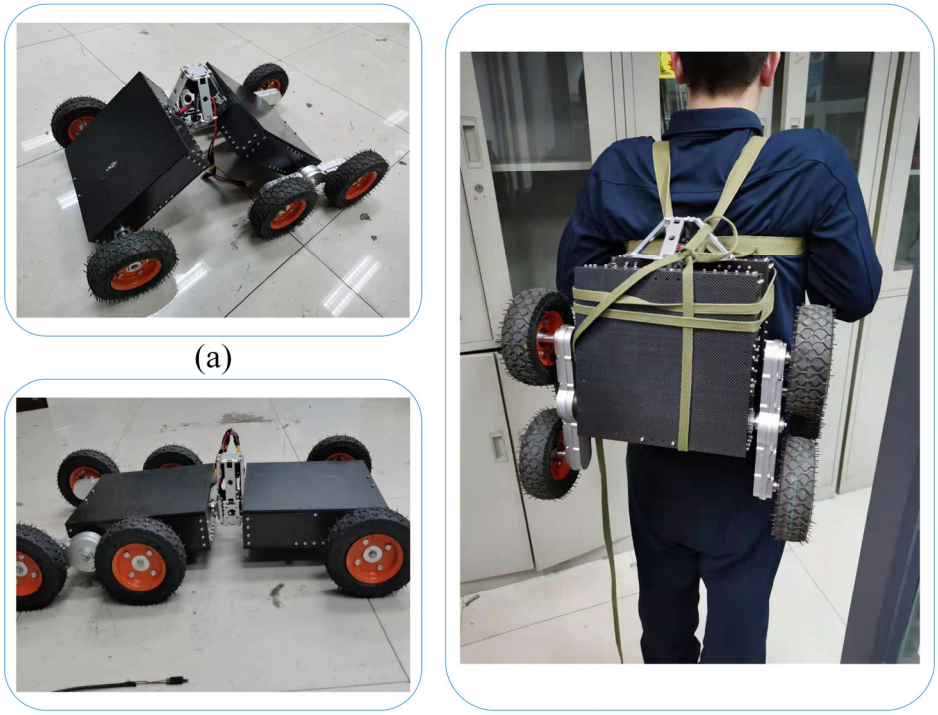

Fig. 14. The physical prototype of the proposed mobile robot. a) The physical prototype is in the V-shaped configuration; b) the physical prototype is in the flat configuration; c) the physical prototype is in the folded configuration.

5.2. Mechatronic and control system of the prototype

As shown in Fig. 15, the mechatronic system of the robot consists of six parts: control system, sensing system, driving components, power system, executing components and robot's mechanical body. The robot's control system is composed of two controllers, one of them is a low-level controller, which is a control board based on a STM32F767 chip (STMicro, Italy and France, see Fig. 16(a)), and the upper one is the remote control or the ground workstation. The motion commands sent by the upper controller are decoded by the signal receiver and then transmitted to the robot's posture control system. After receiving the signal, combined with the robot's posture measured by the nine-axis sensor JY901 (WitMotion, China, see Fig. 16(b)), the posture control system sends the PWM signals and controls the five motors of the robot through the driving components. Driven by the executing components, the robot moves and then feeds back the robot's status information (posture, battery remaining capacity, GPS and so on) and the camera's view to the workstation. The whole mechatronic system is powered by a 24 V lithium battery.

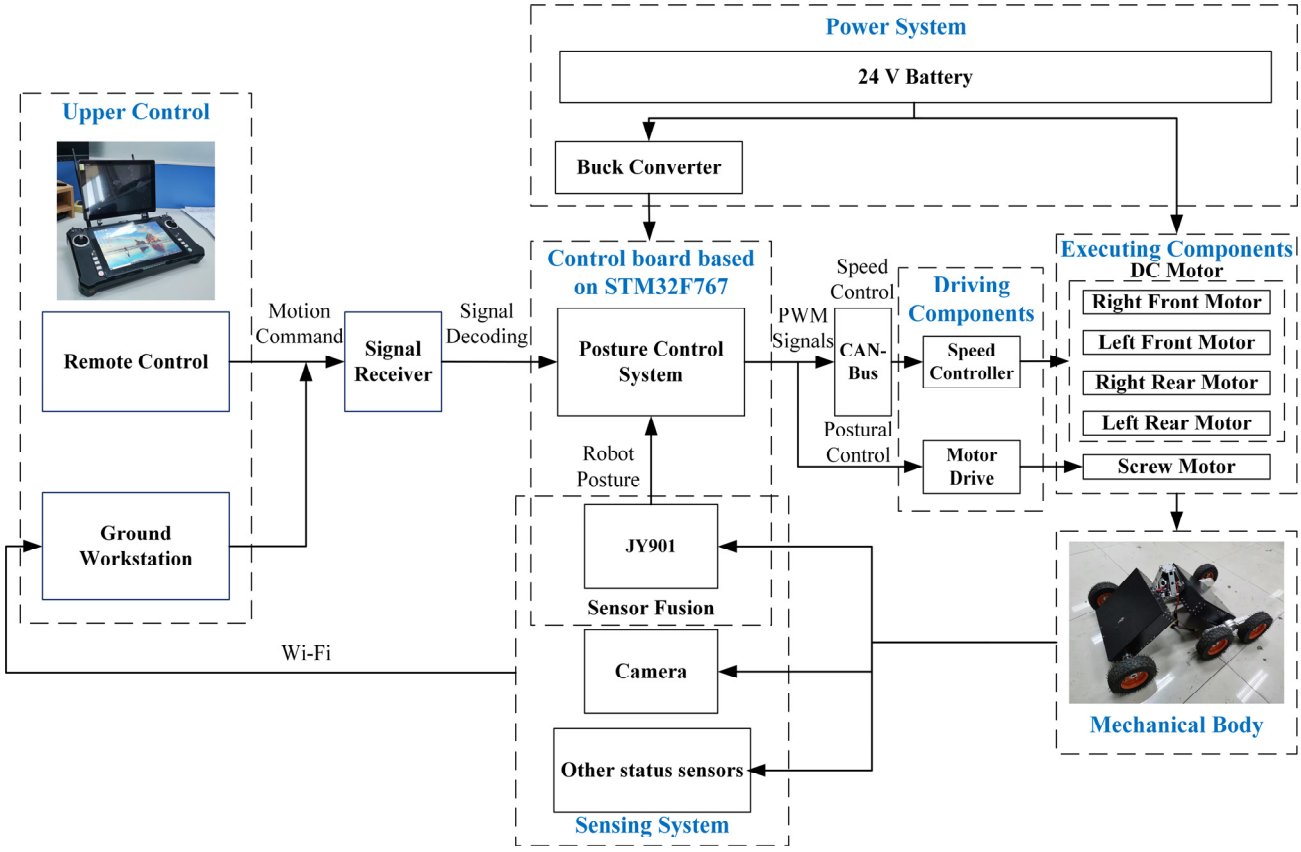

Fig. 15. The structure of the robot's mechatronic system.

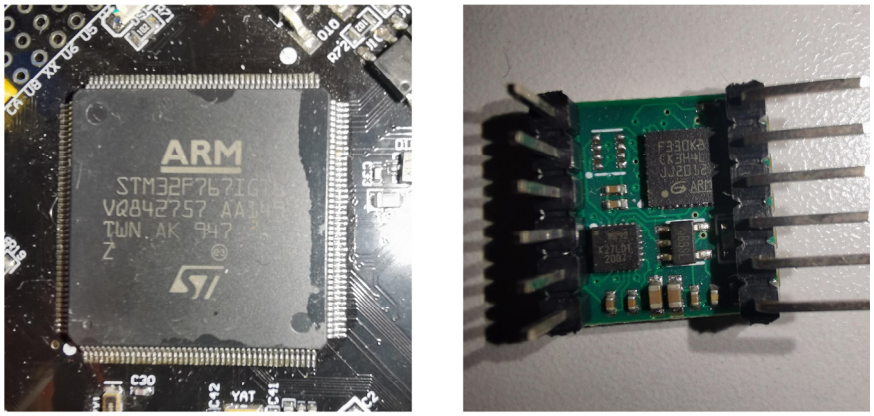

(a) (b)

Fig. 16. The hardware of the proposed mobile robot. a) STM32F767; b) JY901.

The robot's upper controller can be a handheld ground workstation (Zhongju Century UAV, China, see Fig. 17(a)) or just a remote control (RadioLink, China). The ground workstation is based on the Windows operating system (Microsoft, America). It can receive the robot's status information uploaded by the sensing system and make them visible for the operator, as shown in Fig. 17(b) (this software is independently developed by us and is also applicable to other robots in our laboratory). According to the information, the operator can control the motion of the robot by pulling the rocking bars.

(a) (b)

Fig. 17. The handheld ground workstation. a) The appearance of the workstation; b) the monitoring interface of the robot's status.

The robot's low-level controller performed five tasks simultaneously to implements the functions of perception, decision-making, control and communication of the robot. All the tasks run on an embedded development board based on a STM32F767 chip simultaneously through the μC/OS-III operating system (Micrium, America). The workflow of the low-level controller is shown in Fig. 18(a). After the robot is started, all kinds of software are initialized first. Then the robot will enable all tasks only after it detects that the connection with the upper controller is normal. The Recive Task is responsible for receiving signals from the upper controller, reading the signal values of each channel and converting them into control commands such as speed and attitude. The Sensor Task is responsible for reading the raw data of sensors such as gyroscope and accelerometer and transmitting it to the Stabilization Task after data processing. The Stabilization Task is the core control task of the system. It receives the control data of the Recive Task and the sensor data of the Sensor Task. As shown in Fig. 18(b), through the PID closed-loop control of the yaw angle and yaw rate of the robot, it distributes and outputs the desired speed of the motors, so as to control the speed and direction of the robot's movement. As shown in Fig. 18(c), the Motor Task mainly completes the PID closed-loop control of the motor's speed. Its input parameters are the control values of motor's desired speed calculated by the Stabilization Task, and it controls the motor's speed by changing the current of the motor. The Transmission Task is responsible for uploading the robot's posture, voltage, current and environmental information to the upper controller, and receiving the parameter update, change and other instructions from the upper controller.

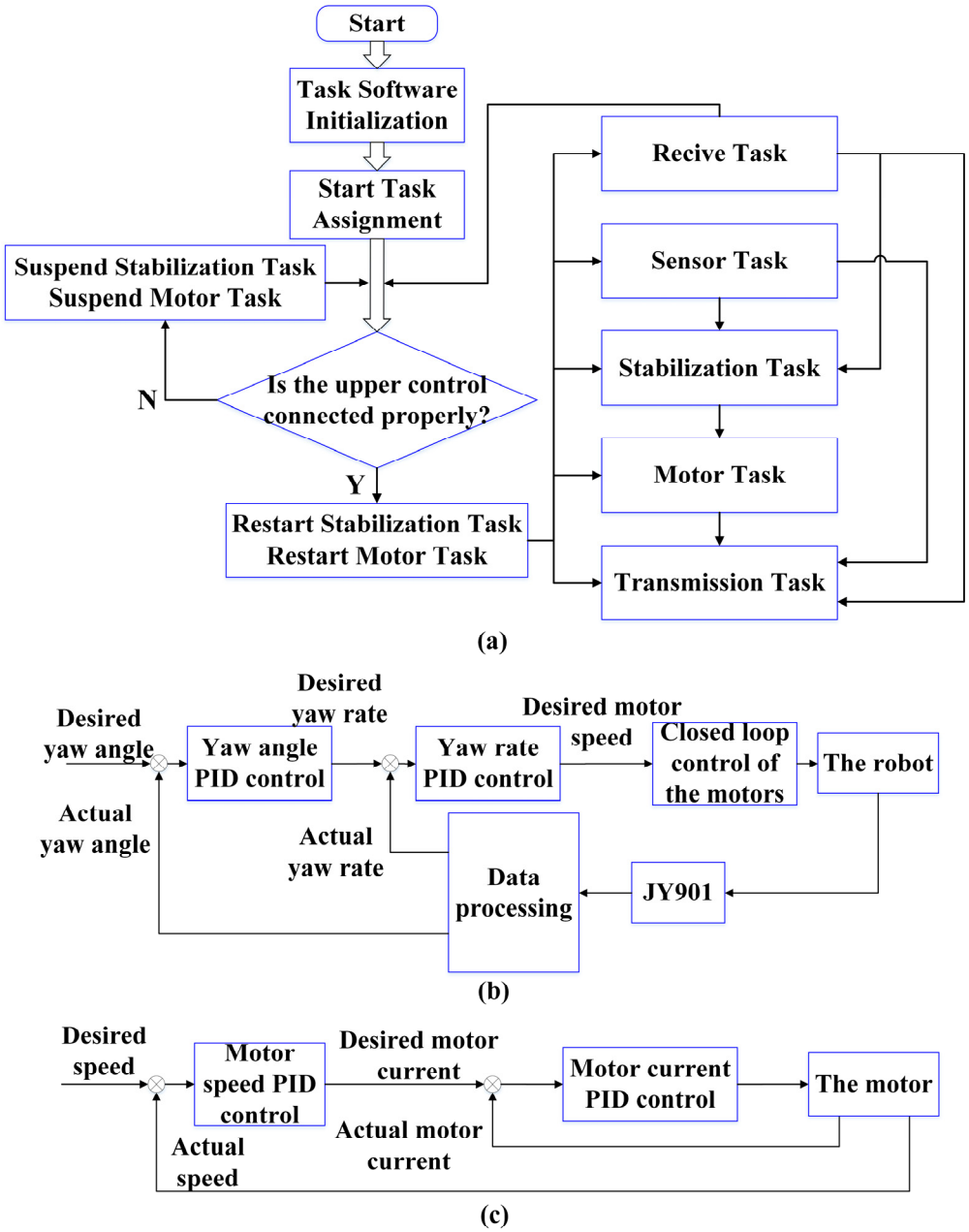

Fig. 18. The composition of the robot's low-level controller. (a) The workflow of the low-level controller; (b) the PID closed-loop control of the yaw angle and yaw rate; (c) the PID closed-loop control of the motor's speed.

5.3. Field experiments of the prototype

Based on the prototype, a series of experiments were carried out to check and verify the performance of the proposed mobile robot. A video for the experiments is available in the supplementary material of this paper.

The first experiment is used to verify the correctness of the derivations in Section 3 and the applicability of the feasible region of δ obtained in the simulation in Section 4. Taking climbing over a 200 mm vertical obstacle as an example, if the variant angles δ are within the corresponding feasible region, the robot can always climb over the obstacle, it is considered that the above derivation and simulation results are correct.

The friction coefficient between the robot's wheel and the obstacle with an aluminium alloy surface is taken as $\mu = 0.4$. Substitute the robot's structural design parameters and vertical obstacle height $h = 200$ mm into $G(\delta)$, $F_1(\delta)$ and $F_2(\delta)$, respectively, and make the image of $G(\delta)$, $F_1(\delta)$ and $F_2(\delta)$ as functions of δ (see Fig. 19) (According to the Fig. 13(c) and Fig. 13(d), when the static conditions are satisfied, the stability condition must also be satisfied. Therefore, the image of $S(\delta)$ doesn't need to be drawn). According to Eqs. (19), (25) and (30), only when $G(\delta)$, $F_1(\delta)$ and $F_2(\delta)$ are greater than 0, the robot can climb the obstacle. It can be seen from Fig. 19 that for a vertical obstacle with a height of 200 mm, the robot can climb the obstacle only when its variant angle δ is greater than 5° and less than 30°.

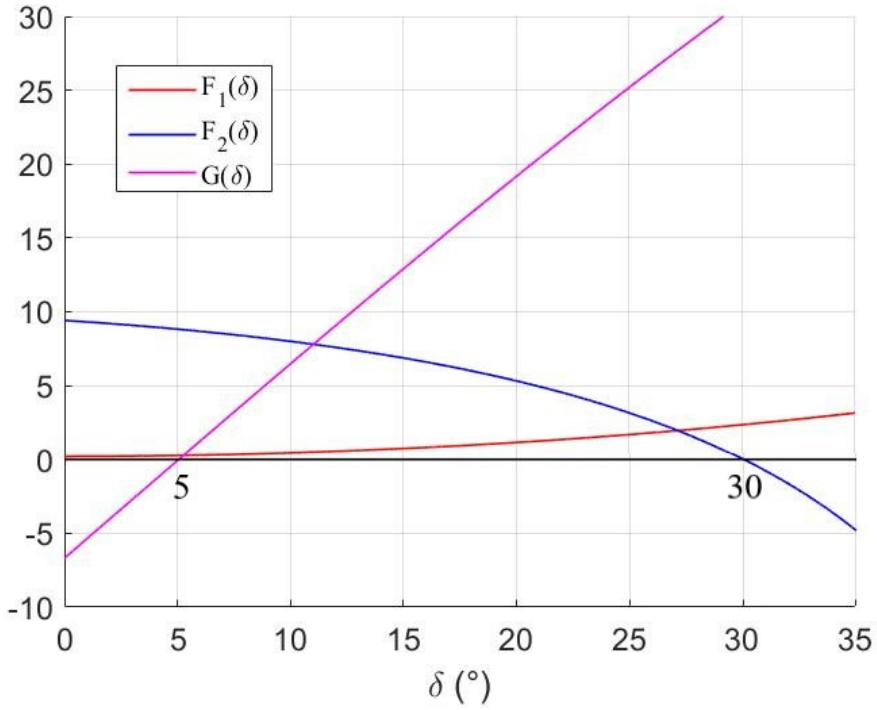

Fig. 19. The values of $G(\delta)$, $F_1(\delta)$ and $F_2(\delta)$ as functions of δ ($h = 200$ mm).

To better compare the experimental results with the simulation results, the variant angles δ of 0°, 10°, 20°, 30° and 50° are taken for experiment and analysis. Substitute the robot's variant angle $\delta = 0°$, 10°, 20°, 30° and 50° into $G(\delta)$, $F_1(\delta)$ and $F_2(\delta)$, and the calculated results are summarized in Table 2. As shown in Fig. 20, to verify the correctness of the simulation results, the robot's obstacle crossing experiments were carried out with the variant angles δ as 0°, 10°, 20°, 30° and 50°, which were measured by the nine-axis sensor JY901. From the experimental results, it can be found that when δ was 0°, the robot did not satisfy the geometric condition. The obstacle-crossing wheels could not touch the top surface of the obstacle and pull the robot (see Fig. 20(a)). When δ was 50°, the robot did not satisfy the static condition and overturned during the obstacle-crossing process (see Fig. 20(b)). When δ was equal to 10°, 20° and 30°, the robot satisfied all the conditions and could climb over the obstacle (see Fig. 20(c), (d) and (e)). Compared to Table 2, it can be seen that the experimental results agreed very well with the simulation results. Therefore, it can be considered that the previous derivation and simulation are correct and consistent with the practical situation.

Table 2 Calculated results of $G(\delta)$, $F_1(\delta)$ and $F_2(\delta)$ with the variant angles δ as 0°, 10°, 20°, 30° and 50°, when h = 200 mm

δ	$G(\delta)$	$F_1(\delta)$	$F_2(\delta)$	Can the robot cross the obstacle?
0°	-6.69 < 0	0.22 > 0	9.41 > 0	No
10°	6.47 > 0	0.45 > 0	8.00 > 0	Yes
20°	19.15 > 0	1.15 > 0	5.33 > 0	Yes
30°	30.92 > 0	2.35 > 0	0.01 > 0	Yes
50°	49.45 > 0	6.44 > 0	-81.07 < 0	No

Fig. 20. The experiment of the robot climbing the 200 mm vertical-high obstacle. (a) The robot climbed the obstacle with δ = 0°; (b) the robot climbed the obstacle with δ = 50°; (c) the robot climbed the obstacle with δ = 10°; (d) the robot climbed the obstacle with δ = 20°; (e) the robot climbed the obstacle

with $\delta = 30°$.

The second experiment is used to test the robot's ability to climb and descend the steps. Firstly, the robot is controlled to climb 140 mm vertical-high continuous steps. Because the steps of the obstacle are made of ceramic tiles, the friction coefficient between the robot's wheels and the obstacle is taken as $\mu = 0.3$. Substitute the robot's structural design parameters and vertical obstacle height $h =$ 140 mm into $F_1(\delta)$ and $F_2(\delta)$, respectively, and make the image of $F_1(\delta)$ and $F_2(\delta)$ as functions of δ (see Fig. 21(a)) (According to Fig. 13(a), the robot always satisfies the geometric constraint when the height of the obstacle is lower than 195 mm. Therefore, there is no need to draw the curve of $G(\delta)$.). According to Eqs. (25) and (30), only when $F_1(\delta)$ and $F_2(\delta)$ are greater than 0, the robot can climb the obstacle. It can be seen from Fig. 21(a) that for a vertical obstacle with a height of 140 mm, the robot can climb the obstacle only when its variant angle δ is greater than 24° and less than 36°.

Therefore, set the variant angle δ to 35° for robot's steps climbing. The experiment of the robot climbing 140 mm vertical-high continuous steps was carried out as shown in Fig. 21(b). During the movement, the robot's front walking wheels always kept in contact with the step surface, and the adaptive climbing rocker legs on both sides of the robot continuously flipped to push the robot to climb the steps. It can be seen that the robot can climb the continuous steps successfully.

Subsequently, the experiment of the robot descending the steps was carried out as shown in Fig. 21(c). During the process, the adaptive rocker legs will rotate adaptively with the steps, so that the front and rear obstacle-crossing wheels of the robot can keep contact with the step surface as much as possible. It can be seen that the robot can descend down the steps.

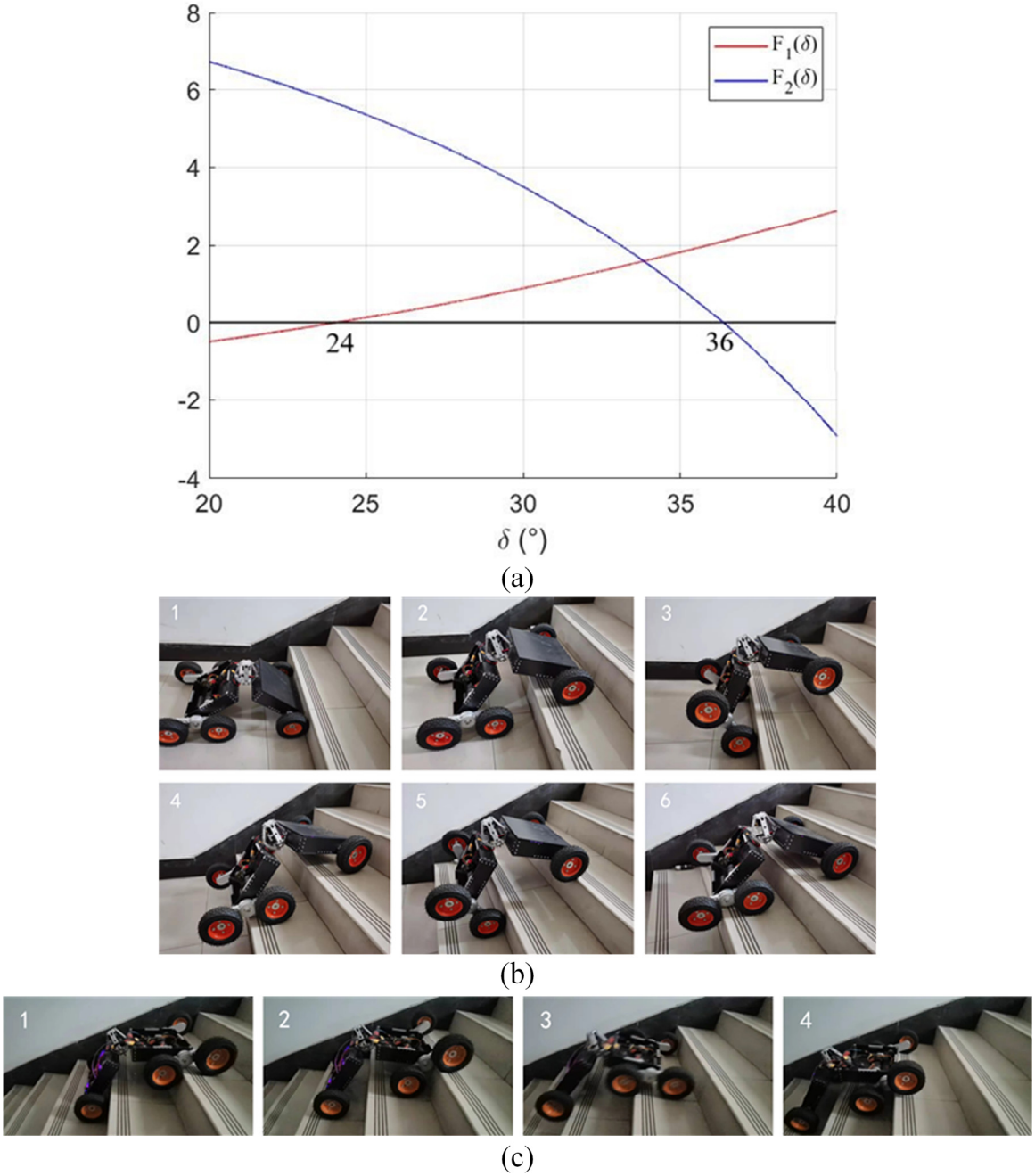

Fig. 21. The experiment of the robot climbing and descending continuous steps. (a) The value of $F_1(\delta)$ and $F_2(\delta)$ as functions of δ (h = 140 mm); (b) the process of the robot climbing the steps; (c) the process of the robot descending the steps.

The third experiment is used to test the robot's ability to climb over irregular obstacles. Fig. 22 shows the process of the robot climbing over a cylindrical obstacle, whose diameter is 190mm. It can be seen that the robot can also climb over the cylindrical obstacle by turning rocker legs, and the process is the same as that of climbing over vertical obstacles.

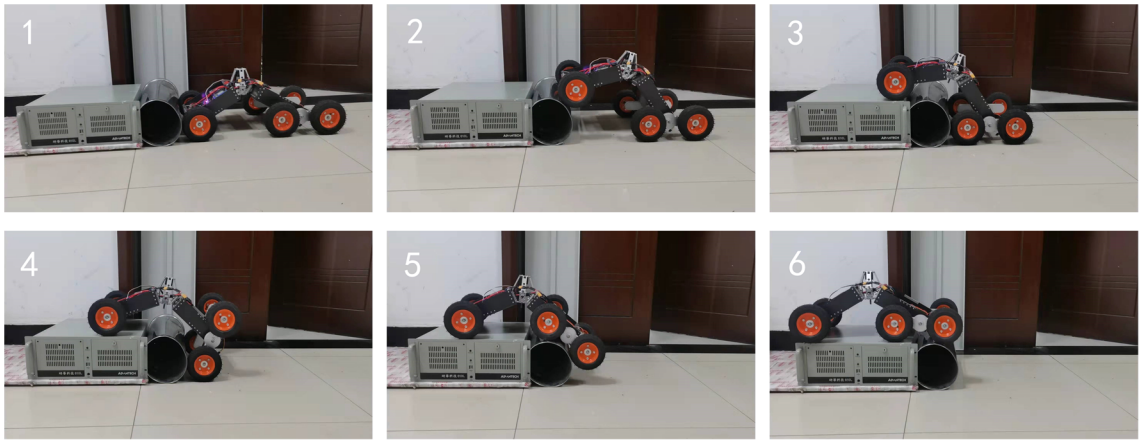

Fig. 22. The experiment of the robot climbing over a cylindrical obstacle.

The fourth experiment is used to test the mobility of the prototype in the field. As shown in Fig. 23, the robot was controlled to climb a slope. Maintaining a low posture, the robot could lower the CoM and prevent itself from overturning. And because of the three-rocker-leg structure, the robot could adapt to the terrain and keep the six wheels always in contact with the ground during the movement, which improved the stability of the robot in the field.

Fig. 23. The robot climbed a slope in the field.

The last experiment is used to verify the terrain adaptability of the prototype in asymmetrical obstacles. As shown in Fig. 24, the robot was crossing a side obstacle. It can be seen that when encountering a side obstacle, relying on its own three-rocker-leg structure, the robot could also keep the wheels in contact with the ground as much as possible in the process of crossing the obstacle, which guaranteed the stability of the robot's motion.

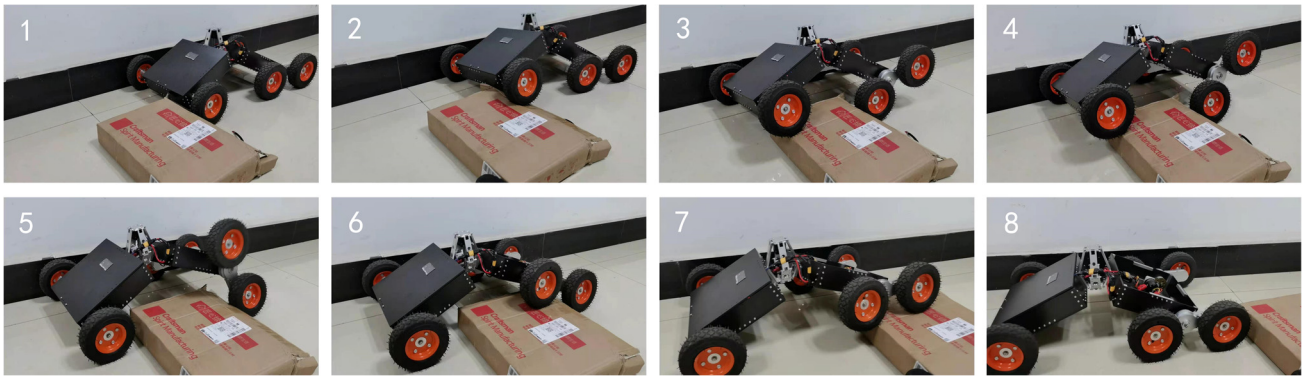

Fig. 24. The robot climbed over a side obstacle.

The experiments accomplished here not only verify the mathematical model, optimization and simulation in this paper, but also show the fact that the robot developed based on the proposed design principles has the distinctive obstacle-crossing capability and terrain adaptability. A video for the above experiments is provided in the supplementary material.

On the basis of experiments, taking some basic features into account, the proposed robot is compared with the other mobile robot listed in Table 3 to evaluate its mobility and other performance [42]. The features include the size, weight, diameter of wheel, max speed, number of wheels, obstacle crossing height and the transformation ratio (the ratio of the maximum obstacle crossing height to the wheels' radius).

It can be found that the proposed mobile robot has excellent obstacle-crossing capability, simple control system and can be folded up for portability. While maintaining an optimum transformation ratio, the robot also has a large obstacle crossing height. The main advantages of the proposed robot are: 1) excellent obstacle crossing capability, the robot can cross obstacles mechanical adaptively without sensing the height and size of the obstacles, therefore, it does not need complex control algorithms; 2) strong terrain adaptability, the robot can keep all six wheels in contact with the ground through its three-rocker-leg structure, which can improve the traction of the wheels and the stability and smoothness of the robot's motion; 3) reconfigurability, the robot can adjust the position of COM, the wheelbase and its own geometric configuration through reconfiguration, so as to improve the geometric and static passing capability. The robot can also be folded up for storage and transportation. In general, the proposed robot has a broad application prospect in disastrous scenarios characterized by uneven terrain and irregularities. In our future work, the dimension and weight of the proposed mobile robot will be reduced.

Table 3 Comparison of some existing mobile robots with the proposed mobile robot

Name	The proposed robot	Epi.q-TG [57]	FlipBot [58]	ASGUARD [50]	Hylos [30, 59]	FUHAR Robot [42]	TurboQuad [43]
Size: Length	780	450	480	950		435	710
Width	454	280	355	500	-	245	370
Height	190	200	160	440		265	160
Weight	9.9 kg	4 kg	7.8 kg	9.5 kg	12 kg	9.5 kg	18.5 kg
Radius of wheel	77.5 mm	30 mm	-	220 mm	-	88.3 mm	105 mm
Max speed	0.5 m/s	-	1 m/s	2 m/s	-	2.2 m/s	0.5 m/s
Number of wheels	6	12	4	4	4	4	4
Obstacle crossing height	At least 200 mm vertical-high obstacle	About 130 mm step in friction conditions (f_s > 1.1)	At least 200 mm square step	At least 170 mm square step	Suitable for rugged terrain	175 mm	At least 145 mm
Transformation ratio	2.58	4.33	-	-	-	1.981	1.07
Portable	Yes	No	No	No	No	-	-
Simple control system	Yes	Yes	Yes	Yes	No	Yes	Yes
Stable equipment platform	Yes	Yes	No	No	Yes	Yes	Yes

6. Conclusions

This paper for the first time presented a novel portable six-wheeled robot with a reconfigurable body and self-adaptable obstacle climbing mechanisms. This robot can transform itself into three locomotion configurations, leading to the terrain adaptability, obstacle climbing ability and portability. It can climb over obstacles of different heights through turning the adaptive climbing rocker legs and adapt to different terrain environments with its three-rocker-leg structure.

The design criteria and mechanical design of the proposed robot were presented. Based on the mechanical design, the geometry of the robot was established and the geometric constraint, static conditions and motion stability condition for obstacle crossing of the robot are derived and formulated. Through numerical simulations, the geometric passing capability, static passing capability and motion stability of the robot were characterized and illustrated, and the feasible region of the structure parameters of the robot in obstacle crossing was identified.

Further, integrated with a mechatronic system and remote control, a physical prototype of the proposed mobile robot was developed. Experiments were subsequently carried out to prove the design concept, feasibility, manoeuvrability of the robot and the above theoretical derivations. The experimental results have verified the simulation results and indicated that the proposed robot was portable, had good obstacle crossing capability and adaptability, which had wide application prospect in disastrous scenarios.

Further research will be focused on the development of an automatic navigation system (the first

prototype is radio-controlled by a human operator) and an energy optimal path planning method to make the robot perform more tasks and more efficiently with limited energy supply.

Appendix A

Table A1 Degrees of freedom of the six-wheeled mobile robot

Number	Type	Description
1	Active	The front body's left DC motor drives the left front walking wheel.
2	Active	The front body's right DC motor drives the right front walking wheel.
3	Active	The screw motor drives the Sarrus-variant mechanism (see Fig.3 for details).
4	Active	The rear body's left DC motor drives the set of obstacle-crossing wheels on the left side (see Fig. 4 for details).
5	Active	The rear body's right DC motor drives the set of obstacle-crossing wheels on the right side (see Fig. 4 for details).
6	Passive	The front body can twist freely relative to the rear body around the connecting shaft (see Fig. 3 for details).
7	Passive	The left adaptive climbing rocker leg can rotate relative to the rear body around the leg's central shaft (see Fig. 4 for details).
8	Passive	The right adaptive climbing rocker leg can rotate relative to the rear body around the leg's central shaft (see Fig. 4 for details).

Nomenclature

Geometrical parameters

B	length between two wheels in the width direction
l_b	length of the front and rear bodies
l_e	length of the adaptive climbing rocker leg
r	radius of the wheels (all the wheels are of the same dimension)
θ_l	swing angle of the left adaptive climbing rocker leg
θ_r	swing angle of the right adaptive climbing rocker leg
θ_f	rotation angle of the coordinate frame $O_4\{X_4, Y_4, Z_4\}$ with respect to the coordinate frame $O_1\{X_1, Y_1, Z_1\}$ in the X_4 - Z_4 plane.
δ	rotation angle of the rear body with respect to the coordinate frame $O_1\{X_1, Y_1, Z_1\}$ in the X_1 - Y_1 plane
α	pitch angle of the robot
β	steer angle of the robot
γ	roll angle of the robot

Mass parameters

m_{fb}	mass of the front body

m_{rb}	mass of the rear body
m_w	mass of the front walking wheel
m_a	mass of the rocker leg
m	overall mass of the robot and $m = m_{fb} + m_{rb} + 2m_w + 2m_a$
Coordinate parameters	
$O_0\{X_0, Y_0, Z_0\}$	fixed inertia frame
$O_1\{X_1, Y_1, Z_1\}$	body coordinate frame located at the intersection of the center line of the robot's rear body and the rotation axe of the rocker legs on both sides
$O_2\{X_2, Y_2, Z_2\}$	body coordinate frame located at the centre point of the left rocker leg
$O_3\{X_3, Y_3, Z_3\}$	body frame located at the centre point of the right rocker leg
$O_4\{X_4, Y_4, Z_4\}$	body frame located at the articulation of the front and rear body (axis Y_4 coincides with the central axis of the rear body and the central axis of the front body is always in the X_4 - Y_4 plane)
${}^0\mathbf{T}_1$	transformation matrix of the robot coordinate frame $O_1\{X_1, Y_1, Z_1\}$ relative to the fixed coordinate frame $O_0\{X_0, Y_0, Z_0\}$
${}^1\mathbf{T}_2$	transformation matrix of the left adaptive climbing rocker leg with respect to the robot coordinate frame $O_1\{X_1, Y_1, Z_1\}$
${}^1\mathbf{T}_3$	transformation matrix of the right adaptive climbing rocker leg with respect to the robot coordinate frame $O_1\{X_1, Y_1, Z_1\}$
${}^1\mathbf{T}_4$	transformation matrix of the front body with respect to the robot coordinate frame $O_1\{X_1, Y_1, Z_1\}$
${}^1\boldsymbol{p}_{fb}$	vector of the centroid of the front body in the robot coordinate frame $O_1\{X_1, Y_1, Z_1\}$
${}^1\boldsymbol{p}_{rb}$	vector of the centroid of the rear body in the robot coordinate frame $O_1\{X_1, Y_1, Z_1\}$
${}^1\boldsymbol{p}_{lw}$	vector of the centroid of the left front walking wheel in the robot coordinate frame $O_1\{X_1, Y_1, Z_1\}$
${}^1\boldsymbol{p}_{rw}$	vector of the centroid of the right front walking wheel in the robot coordinate frame $O_1\{X_1, Y_1, Z_1\}$
${}^1\boldsymbol{p}_2$	vector of the centroid of the left adaptive climbing rocker leg in the robot coordinate frame $O_1\{X_1, Y_1, Z_1\}$
${}^1\boldsymbol{p}_3$	vector of the centroid of the right adaptive climbing rocker leg in the robot coordinate frame $O_1\{X_1, Y_1, Z_1\}$
${}^1\boldsymbol{P}$	vector of the centroid of the robot in the robot coordinate frame $O_1\{X_1, Y_1, Z_1\}$
${}^0\boldsymbol{P}$	vector of the centroid of the robot in the fixed coordinate frame $O_0\{X_0, Y_0, Z_0\}$
Static parameters	
N_1	supporting force of the obstacle on the front walking wheel
N_2	supporting force of the ground against the front obstacle-crossing wheel
N_3	supporting force of the ground against the rear obstacle-crossing wheel
N_4	supporting force of the obstacle on the front obstacle-crossing wheel
N_5	supporting force of the ground against the front walking wheel
f_1	friction force of the obstacle on the front walking wheel
f_2	friction force of the ground against the front obstacle-crossing wheel
f_3	friction force of the ground against the rear obstacle-crossing wheel
f_4	friction force of the obstacle on the front obstacle-crossing wheel

f_5	friction force of the ground against the front walking wheel
T	torque of the rocker leg's center shaft.
i_{73}	transmission ratio between the wheel shaft 7 and the sun gear 3 in Fig. 4(b)

Simulation parameters

$G(\delta)$	function of the geometric passing capability for obstacle crossing
$F_1(\delta)$, $F_2(\delta)$	function of the static passing capability for obstacle crossing
$S(\delta)$	function of the motion stability for obstacle crossing
h_{max0}	maximum obstacle crossing height of the robot satisfying geometric passing capability at the current rear body pitch angle δ
δ_{min}	minimum rear body pitch angle at which the robot can lift the front body in the obstacle-crossing phase (b) under the current friction coefficient μ
h_{max1}	maximum obstacle crossing height of the robot satisfying the torque condition under the current rear body pitch angle δ and friction coefficient μ
h_{max2}	maximum obstacle crossing height of the robot satisfying the static stability condition under the current rear body pitch angle δ

Mathematical symbols

A_1	$A_1 = \arccos \dfrac{(h-r)^2 + l_e^{\,2}}{2l_e\sqrt{(h-r)^2 + r^2}}$
A_2	$A_2 = \arccos \dfrac{r}{\sqrt{(h-r)^2 + r^2}}$
A_3	$A_3 = (f_2 + f_3)r$
A_4	$A_4 = f_1(r + 2l_b\cos\delta)$
A_5	$A_5 = 2N_1 l_b \cos\delta\cos\alpha$
A_6	$A_6 = f_1(2l_b\cos\delta\sin\alpha - r)$
A_7	$A_7 = \dfrac{M_1 g l_b \cos\delta\cos\alpha}{2}$
A_8	$A_8 = \dfrac{M_2 g l_b \sin\delta\sin\alpha}{2}$
A_9	$A_9 = \sqrt{(l_b\cos\delta)^2 - \left(\dfrac{h}{2}\right)^2}$
A_{10}	$A_{10} = \sqrt{\dfrac{l_e^{\,2}}{4} - (h - 2l_b\cos\delta\sin\alpha)^2}$
M_1	$M_1 = 3m_{fb} + m_{rb} + 8m_w$
M_2	$M_2 = m_{fb} + m_{rb}$

References

[1] S. Tadokoro, T. Takamori, S. Tsurutani, and K. Osuka, "On Robotic Rescue Facilities for Disastrous Earthquakes -From the Great Hanshin-Awaji (Kobe) Earthquake," *Journal of Robotics Mechatronics,* vol. 9, no. 1, pp. 46-56, 1997.

[2] J. Casper and R. R. Murphy, "Human-robot interactions during the robot-assisted urban search and rescue response at the World Trade Center," *IEEE Transactions on Systems Man Cybernetics Part B Cybernetics A Publication of the IEEE Systems Man Cybernetics Society,* vol. 33, no. 3, p. 367, 2003.

[3] A. Meghdari, H. N. Pishkenari, A. L. Gaskarimahalle, S. H. Mahboobi, and R. Karimi, "A Novel Approach for Optimal Design of a Rover Mechanism," *Journal of Intelligent Robotic Systems,* vol. 44, no. 4, pp. 291-312, 2005.

[4] K. Nagatani, A. Yamasaki, K. Yoshida, and T. Adachi, "Development and Control Method of Six-Wheel Robot with Rocker Structure," in *Safety, Security and Rescue Robotics, 2007. SSRR 2007. IEEE International Workshop on*, 2007.

[5] Y. Zhu, Y. Fei, and H. Xu, "Stability Analysis of a Wheel-Track-Leg Hybrid Mobile Robot," *Journal of Intelligent Robotic Systems,* vol. 91, no. 2, 2017.

[6] F. Michaud *et al.*, "Multi-Modal Locomotion Robotic Platform Using Leg-Track-Wheel Articulations," *Autonomous Robots,* vol. 18, no. 2, pp. 137-156, 2005.

[7] Z. Luo, J. Shang, G. Wei, and L. Ren, "A reconfigurable hybrid wheel-track mobile robot based on Watt II six-bar linkage," *Mechanism Machine Theory,* vol. 128, no. 10, pp. 16-32, 2018.

[8] Y. Li *et al.*, "Development and applications of rescue robots for explosion accidents in coal mines," *Journal of Robotic Systems,* vol. 37, no. 3, pp. 466-489, 2020.

[9] R. Buchanan, L. Wellhausen, M. Bjelonic, T. Bandyopadhyay, and M. Hutter, "Perceptive Whole Body Planning for Multi-legged Robots in Confined Spaces," *Journal of Field Robotics,* no. 3, 2020.

[10] L. Bruzzone and G. Quaglia, "Review article: locomotion systems for ground mobile robots in unstructured environments," *Mechanical Sciences,* vol. 3, no. 2, pp. 49-62, 2012.

[11] M. Ning *et al.*, "Design and analysis for a multifunctional rescue robot with four-bar wheel-legged structure," *Advances in Mechanical Engineering,* vol. 10, no. 2, pp. 1-14, 2018.

[12] L. Bruzzone and P. Fanghella, "Mantis: hybrid leg-wheel ground mobile robot," *Industrial Robot: An International Journal,* vol. 41, no. 1, pp. 26 - 36, 2014.

[13] S. Amiri *et al.*, "Emirates Mars Mission (EMM) 2020 Overview," presented at the EGU General Assembly Conference Abstracts, April 2017.

[14] Y. Zhang, J. Xiao, X. Zhang, D. Liu, and H. Zou, "Design and implementation of Chang'E-3 rover location system," *Scientia Sinica Technologica,* vol. 44, no. 5, p. 483, 2014.

[15] R. A. Lindemann and C. J. Voorhees, "Mars Exploration Rover mobility assembly design, test and performance," in *IEEE International Conference on Systems*, 2006, vol. 1.

[16] S. W. Squyres and G. Crater, "The Spirit Rover's Athena Science Investigation at Gusev Crater, Mars," *Science,* vol. 305, no. 5685, pp. 794-799, 2004.

[17] D. Kim, H. Hong, H. S. Kim, and J. Kim, "Optimal design and kinetic analysis of a stair-climbing mobile robot with rocker-bogie mechanism," *Mechanism Machine Theory,* vol. 50, no. none, pp. 90-108, 2012.

[18] R. Kozma, T. Hunstberger, H. Aghazarian, and W. J. Freeman, "Implementing intentional robotics principles using SSR2K platform," in *IEEE/RSJ International Conference on Intelligent Robots & Systems*, 2007.

[19] R. Kozma, T. Huntsberger, H. Aghazarian, E. Tunstel, R. Ilin, and W. Freeman, "Intentional Control for Planetary Rover SRR," *Advanced Robotics,* vol. 22, no. 12, pp. 1309-1327, 2008.

[20] T. Aoki, Y. Murayama, and S. Hirose, "Development of a Transformable Three-wheeled Lunar Rover: Tri-Star IV," *Journal of Field Robotics,* vol. 31, no. 1, pp. 206-223, 2013.

[21] D. Wettergreen, D. Jonak, D. Kohanbash, and J. Teza, "Design and field experimentation of a prototype Lunar prospector," *The International Journal of Robotics Research,* 2010.

[22] H. Jiang, G. Xu, W. Zeng, and F. Gao, "Design and kinematic modeling of a passively-actively transformable mobile robot," *Mechanism Machine Theory,* vol. 142, pp. 103591-, 2019.

[23] R. Siegwart, P. Lamon, T. Estier, M. Lauria, and R. Piguet, "Innovative design for wheeled locomotion in rough terrain," *Robotics Autonomous Systems,* vol. 40, no. 2-3, pp. 151-162, 2000.

[24] M. Ning *et al.*, "Design, Analysis, and Experiment for Rescue Robot with Wheel-Legged Structure," *Mathematical Problems in Engineering,* 2017.

[25] M. Lacagnina, G. Muscato, and R. Sinatra, "Kinematics, dynamics and control of a hybrid robot Wheeleg," *Robotics Autonomous Systems,* vol. 45, no. 3-4, pp. 161-180, 2003.

[26] D. Lu, E. Dong, C. Liu, X. Min, and Y. Jie, "Design and development of a leg-wheel hybrid robot "HyTRo-I"," in *IEEE/RSJ International Conference on Intelligent Robots and Systems*, 2013.

[27] D. Lu, E. Dong, C. Liu, M. Xu, and J. Yang, "Generation and Analyses of the Reinforced Wave Gait for a Mammal-Like Quadruped Robot," *Journal of Intelligent Robotic Systems,* vol. 82, no. 1, pp. 51-68, 2016.

[28] V. Krovi and V. Kumar, "Modeling and Control of a Hybrid Locomotion System," *Journal of Mechanical Design,* vol. 121, no. 3, pp. 448-455, 1999.

[29] Q. Chang, X. Liu, W. Xu, Y. Lei, and B. Yang, "The design and experiments of a small wheel-legged mobile robot system with two robotic arms," in *2016 IEEE/RSJ International Conference on Intelligent Robots and Systems (IROS)*, 2016.

[30] C. Grand, F. Benamar, and F. Plumet, "Motion kinematics analysis of wheeled-legged rover over 3D surface with posture adaptation," *Mechanism Machine Theory,* vol. 45, no. 3, pp. 477-495, 2010.

[31] M. Lauria, Y. Piguet, and R. Siegwart, "Octopus - An Autonomous Wheeled Climbing Robot " presented at the The Fifth International Conference on Climbing and Walking Robots (CLAWAR), Paris, France, September 25-27, 2002.

[32] B. H. Wilcox, "ATHLETE: A cargo-handling vehicle for solar system exploration," *IEEE Aerospace Conference,* 2011.

[33] V. Sunspiral, D. W. Wheeler, D. Chavez-Clemente, and D. Mittman, "Development and field testing of the FootFall planning system for the ATHLETE robots," *Journal of Field Robotics,* vol. 29, no. 3, pp. 483-505, 2012.

[34] F. Cordes, A. Dettmann, and F. Kirchner, "Locomotion modes for a hybrid wheeled-leg planetary rover," presented at the 2011 IEEE International Conference on Robotics and Biomimetics, 2011.

[35] T. M. Roehr, F. Cordes, and F. Kirchner, "Reconfigurable Integrated Multirobot Exploration System (RIMRES): Heterogeneous Modular Reconfigurable Robots for Space Exploration," *Journal of Field Robotics,* vol. 31, no. 1, pp. 3-34, 2013.

[36] A. Halme, I. Leppnen, and S. Salmi, "Development of WorkPartner-robot - Design of actuating and motion control system," 1999.

[37] Y. Seong-Ho, P. Jaehyun, S. Jiwon, and K. Yong-Jae, "Development of an Agile Omnidirectional Mobile Robot with GRF Compensated Wheel-Leg Mechanisms for Human Environments," *IEEE Robotics and Automation Letters,* 2021.

[38] A. Alamdari, R. Herin, and V. N. Krovi, "Quantitative Kinematic Performance Comparison Of Reconfigurable Leg-Wheeled Vehicles," in *Nature-Inspired Mobile Robotics*, 2013, pp. 585-592.

[39] A. Alamdari and V. N. Krovi, "Static balancing of highly reconfigurable articulated wheeled vehicles for power consumption reduction of actuators," *International Journal of Mechanisms and Robotic Systems,* vol. 3, no. 1, pp. 15-31, 2016.

[40] S. C. Chen, J. H. Ke, C. H. Li, and P. C. Lin, "Trajectory planning for stair climbing in the leg-wheel hybrid mobile robot quattroped," in *IEEE International Conference on Robotics & Automation*, 2011.

[41] S.-C. Chen, K.-J. Huang, W.-H. Chen, S.-Y. Shen, and C.-H. Li, "Quattroped: A Leg--Wheel Transformable Robot," *IEEE/ASME Transactions on Mechatronics,* vol. 19, no. 2, pp. 730-742, 2013.

[42] R. Mertyüz, A. K. Tanyldz, B. Taar, A. B. Tatar, and O. Yakut, "FUHAR: A transformable wheel-legged hybrid mobile robot," *Robotics Autonomous Systems,* vol. 133, 2020.

[43] W. H. Chen, H. S. Lin, Y. M. Lin, and P. C. Lin, "TurboQuad: A Novel Leg–Wheel Transformable Robot With Smooth and Fast Behavioral Transitions," *IEEE Transactions on Robotics,* vol. 33, no. 5, pp. 1025-1040, 2017.

[44] C. Zheng and K. Lee, "WheeLeR: Wheel-Leg Reconfigurable Mechanism with Passive Gears for Mobile Robot Applications," in *2019 International Conference on Robotics and Automation (ICRA)*, 2019, pp. 9292-9298.

[45] Y. Kim, L. Lee, S. Lee, J. Kim, H. S. Kim, and T. W. Seo, "STEP: A New Mobile Platform With 2-DOF Transformable Wheels for Service Robots," *IEEE/ASME Transactions on Mechatronics,* vol. 25, no. 4, pp. 1859-1868, 2020.

[46] K. Tadakuma, R. Tadakuma, A. Maruyama, E. Rohmer, and M. Kaneko, "Mechanical design of the Wheel-Leg hybrid mobile robot to realize a large wheel diameter," in *IEEE/RSJ International Conference on Intelligent Robots & Systems*, 2010.

[47] D. Wang, "Design and Research of Mobile robot with Transformable Wheels," Beijing Jiaotong University, 2016.

[48] S. D. Herbert, A. Drenner, and N. Papanikolopoulos, "Loper: A quadruped-hybrid stair climbing robot," in *IEEE International Conference on Robotics & Automation*, 2008.

[49] R. Altendorfer, N. Moore, H. Komsuoglu, M. Buehler, and D. E. Koditschek, "RHex: A Biologically Inspired Hexapod Runner," *Autonomous Robots,* vol. 11, no. 3, pp. 207–213, 2001.

[50] K. J. Waldron, M. Eich, F. Grimminger, and F. Kirchner, "Adaptive compliance control of a multi-legged stair-climbing robot based on proprioceptive data," *Industrial Robot,* vol. 36, no. 4, pp. 331-339, 2009.

[51] G. Quaglia and M. Nisi, "Design and Construction of a New Version of the Epi.q UGV for Monitoring and Surveillance Tasks," in *ASME 2015 International Mechanical Engineering Congress and Exposition*, 2015.

[52] G. Quaglia, L. Bruzzone, R. Oderio, and R. P. Razzoli, "Epi.q Mobile Robots Family," in *Asme International Mechanical Engineering Congress & Exposition*, 2011, pp. 1165-1172.

[53] R. Oderio and G. Quaglia, "Design of the small mobile robot Epi.q-2," presented at the Proceedings of the XIX Congress AIMETA - Italian Association for Theoretical and Applied Mechanics, 2009.

[54] G. Chen, S. Zhang, and G. Li, "Multistable Behaviors of Compliant Sarrus Mechanisms," *Journal of Mechanisms Robotics,* vol. 5, no. 2, pp. 021005-1-021005-10, 2013.

[55] C. Liu, "Research on obstacle-performance of articulated-track inspection robot under complex environment," University of South China, 2018.

[56] E. Garcia, J. Estremera, and P. Santos, "A comparative study of stability margins for walking machines," *Robotica,* vol. 20, no. part 6, pp. p.595-606, 2002.

[57] G. Quaglia, L. Bruzzone, G. Bozzini, R. Oderio, and R. P. Razzoli, "Epi.q-TG: mobile robot for surveillance," *Industrial Robot,* vol. 38, no. 3, pp. 282-291, 2011.

[58] S. ByungHoon, K. HyunGyu, K. MinHyeok, J. Kyungmin, and S. TaeWon, "FlipBot: A new field robotic platform for fast stair climbing," *International Journal of Precision Engineering & Manufacturing,* vol. 14, no. 11, pp. 1909-1914, 2013.

[59] C. Grand, F. Benamar, F. Plumet, and P. Bidaud, "Decoupled control of posture and trajectory of the hybrid wheel-legged robot Hylos," in *IEEE International Conference on Robotics & Automation*, 2004.